Twenty-Year Climatology of Solar UV and PAR in Cyprus: Integrating Satellite Earth Observations with Radiative Transfer Modeling

Konstantinos Fragkos *, Ilias Fountoulakis, Georgia Charalampous, Kyriakoula Papachristopoulou, Argyro Nisantzi, Diofantos GI. Hadjimitsis, Stelios Kazadzis

Posted Date: 5 April 2024

doi: 10.20944/preprints202404.0431.v1

Keywords: Ultraviolet Radiation; Erythema; UV-Index; Photosynthetically Active Radiation

Article

Twenty-Year Climatology of Solar UV and PAR in Cyprus: Integrating Satellite Earth Observations with Radiative Transfer Modeling

Konstantinos Fragkos [1,*], Ilias Fountoulakis [2,3], Georgia Charalampous [1,4], Kyriakoula Papachristopoulou [2], Argyro Nisantzi [1,4], Diofantos Hadjimitsis [1,4] and Stelios Kazadzis [5]

[1] Eratosthenes Centre of Excellence, Fragklinou Rousvelt 82, 3012 Limassol, Cyprus
[2] Institute for Astronomy, Astrophysics, Space Applications and Remote Sensing, National Observatory of Athens (IAASARS/NOA), GR15236 Athens, Greece
[3] Research Centre for Atmospheric Physics and Climatology, Academy of Athens, 106 79 Athens, Greece
[4] Department of Civil Engineering & Geomatics, Cyprus University of Technology, 3036 Limassol, Cyprus
[5] Physikalisch-Meteorologisches Observatorium Davos, World Radiation Center (PMOD/WRC), Davos 7260, Switzerland
* Correspondence: kostas.fragkos@eratosthenes.org.cy

Abstract: In this study, we present comprehensive climatologies of effective ultraviolet (UV) quantities and photosynthetically active radiation (PAR) over Cyprus for the period 2004 to 2023, leveraging the synergy of earth observation (EO) data and radiative transfer model simulations. The EO dataset, encompassing satellite and re-analysis data for aerosols, total ozone column, and water vapor, alongside cloud modification factors, to capture the nuanced dynamics of Cyprus's atmospheric conditions. With a temporal resolution of 15 minutes and a spatial of 0.05°x0.05°, these climatologies undergo rigorous validation against established satellite datasets and are further evaluated through comparisons with ground-based global horizontal irradiance measurements provided by the Meteorological Office of Cyprus. This dual-method validation approach not only underscores the models' accuracy but also highlights their proficiency in capturing intra-daily cloud coverage variations. Our analysis extends to investigating the long-term trends of these solar radiation quantities, examining their interplay with changes in cloud attenuation, aerosol optical depth (AOD), and total ozone column (TOC). Significant decreasing trends in the noon ultraviolet index (UVI), of -2 to -4% per decade have been found in Autumn, especially marked on the island's Northeastern part, mainly originating from the (significant) positive trends in TOC. The significant decreasing trends in TOC, of -2 to -3% per decade that were found in Spring do not result in correspondingly significant positive trends in the noon UVI since variations in cloudiness and aerosols also have a strong impact on the UVI in this season. The seasonal trends in the Daylight Integral (DLI) were generally not significant. These insights provide a valuable foundation for further studies aimed at developing public health strategies and enhancing agricultural productivity, highlighting the critical importance of accurate and high-resolution climatological data.

Keywords: ultraviolet radiation; erythema; UV-index; photosynthetically active radiation

1. Introduction

Sunlight is a crucial element for the development and sustainability of life on Earth. The sun emits radiation that closely resembles a blackbody with a temperature of approximately 5800 K. This radiation covers a wide spectral range, ranging from about 2 nm (x-rays) to up to 10 meters (radio waves), with its peak emission at approximately 550 nm. The Earth's atmosphere acts as a protective

 doi:10.20944/preprints202404.0431.v1

shield, preventing highly energetic photons with wavelengths shorter than 290 nm from reaching the Earth's surface. The solar spectrum can be divided into narrower regions, each of which has distinct effects on ecosystems and humans. About half of the total solar radiation is in the visible spectral region. Of particular significance for life on Earth are two key regions: the ultraviolet (UV) and the visible spectrum (VIS).

Plants utilize radiation in the VIS region for photosynthesis, with photosynthetically active radiation (PAR) defined as the radiation within the 400 – 700 nm spectral range [1–3]. Exposure to PAR (as well as UV radiation) significantly influences plant health and growth, and variations in PAR levels can impact both terrestrial and marine fauna [4–6]. These impacts have direct impact on the functionality and health of ecosystems, as well as on the food production for humans. PAR controls biomass productivity through photosynthesis and plays a vital role in carbon and water cycles (e.g., [7]). Consequently, is a key variable in global ecosystem and Earth system modeling (e.g., [8]). Nevertheless, ground-based PAR measurements are sparse and thus it is commonly estimated either from measurements of the SSR using empirical equations (e.g., [9–11]) or from satellite observations (e.g., [12]).

Ultraviolet (UV) encompasses wavelengths ranging from 100 – 400 nm. Based on its biological activity and the extent to which it can penetrate the human skin, UV radiation is further classified into three narrower bands: UV-C (100 – 280 nm), UV-B (280 – 315 nm), and UV-A (315 – 400 nm). Despite constituting only 9.3% of the emitted solar radiation [13], and an even smaller fraction of the surface solar radiation (SSR) [14,15], UV radiation carries significant biological implications (e.g., [16–18]). UV-C radiation is hazardous to living organisms but is effectively absorbed in the upper atmosphere by molecular oxygen and other atmospheric constituents, preventing its entry into the troposphere. Most UV-B is also absorbed by molecular oxygen and stratospheric ozone, with only photons having wavelengths longer than 295 nm reaching the Earth's surface. UV-A radiation, on the other hand, enters the troposphere, where it is strongly scattered by air molecules and aerosols.

Excessive exposure to UV radiation can lead to erythema and burns to the human skin [19]. Systematic overexposure to UV stands as a primary environmental risk factor for non-melanoma skin cancer and is among the key contributors to melanoma skin cancer [20,21], along with eye cataract [22]. In contrast, moderate UV exposure is beneficial for humans, as it is essential for the production of vitamin D in the human skin [23–25]. Additionally, it contributes to the maintenance of good mental health and can aid in the treatment of certain diseases [26]. The UV index (UVI) [27] is a common metric used to quantify the potential of UV radiation to cause erythema on human skin. Another important metric is the effective dose to produce vitamin D (VID) [28], which measures the potential of solar UV radiation to stimulate vitamin D production in the human skin [29]. While UV radiation is essential for various physiological processes, it can also damage DNA, which underscores the complex nature of its effects on human health [30]. However, it's essential to note that the positive and negative impacts of UV exposure, relative to exposure time (for a given intensity), also strongly depend on individual physiological factors such as skin type [31].

Similarly, UV radiation has significant effects on plant life, influencing both growth and development. While moderate levels of UV-B radiation can stimulate certain beneficial responses in plants growth [PLG], such as enhanced production of secondary metabolites that can protect against pests and diseases [32], excessive UV exposure can cause plant damage [PLD] including DNA damage, inhibition of photosynthesis, and impaired growth and development [33]. Plants have developed various adaptive mechanisms to cope with UV stress, including the production of UV-absorbing compounds and repair processes for UV-induced DNA damage [34].

Over the past few decades, there have been substantial variations in UV-B radiation levels, which consequently affect UVI and VID, across densely populated mid-latitude regions. In the 1980s and early 1990s, several studies reported an increase in UV-B levels attributed to severe depletion of stratospheric ozone [35–39]. However, the implementation of the Montreal Protocol in 1987 resulted in a drastic reduction in emissions of anthropogenic ozone-depleting substances (ODSs), which were the primary contributors to this issue. Since the mid-1990s the upper stratospheric ozone has been recovering due to the decline in ODSs. Nevertheless, the lower stratospheric ozone has experienced

 doi:10.20944/preprints202404.0431.v1

a decline over the past two decades, possibly influenced by climatic changes [40]. A recent study [41] showed that the decreasing lower stratospheric ozone levels over Rome, Italy have led to negative trends in total ozone and, have directly impacted UV-B radiation trends from 1996 to 2020. Furthermore, changes in aerosols and cloud cover have been identified as the primary drivers of fluctuations in UV radiation at specific mid-latitude locations [42–46]. These same factors also impact the SSR and, consequently, PAR. Statistically significant trends in SSR over the past 2 to 4 decades have been reported at various Mediterranean sites, primarily due to shifts in cloud cover and aerosol loading [47–51]. Anthropogenic climate changes are expected to further influence the key factors affecting PAR and UV, particularly in the Mediterranean basin, which is considered a climate-change hotspot [52,53].

Changes in PAR and UV have a direct impact on key economic sectors in Cyprus, such as the agriculture and tourism. While a study [54] reported a statistically significant increase in SSR over Cyprus at a rate of approximately 2% per decade from 2004 to 2017, there is currently no comprehensive research documenting the corresponding changes in UV and PAR. Although changes in SSR can provide valuable insights into the direction of changes in PAR (though not necessarily UV), it is crucial to note that the magnitude of these changes can vary significantly due to differences in how VIS and UV photons interact with aerosols, clouds, and water vapor, relative to the interactions of the same factors with SSR, which primarily consists of near-infrared (NIR) radiation. Climatological data for PAR and UVI are available at specific monitoring stations on the island [55–58]. However, these records are not continuous since 2004, and their applicability is limited due to Cyprus's complex topography, which can result in regional variations. Based on state-of-the-art reanalysis and satellite information we constructed a high spatial and temporal resolution climatology of the UVI, the VID and the PAR for 2004 – 2023 which can be of interest for research in various sectors (e.g., health, tourism, agriculture). We also tried to estimate the trends in these quantities with respect to the main factors affecting them.

The paper is organized as follows: The first section introduces the subject matter, underscoring the significance of PAR and UV radiation in environmental and health contexts. Following this, the second section details the data sources utilized in this study and delineates the methodologies employed for their analysis. The third section is devoted to presenting the core results, accompanied by a thorough discussion of the insights they yield. The paper culminates with the fourth and final section, which encapsulates the summary of the research and distils the principal conclusions drawn from the study's outcomes.

2. Materials and Methods

2.1. Data Processing

Radiometric quantities (UVI, VID, DNA, PLD, PLG and PAR) were simulated for the time frame spanning from 2004 to 2020, covering the geographical region between 34°N – 36°N, 32°E – 36°E. These simulations were carried out with a temporal resolution of 15 mins and a fine spatial resolution of 0.05° x 0.05°. Different Look Up Table (LUTs) were used to achieve the completion of the simulations of all quantities on such fine spatial and temporal resolution. The parameterization of the LUT for the effective UV doses is not the same as the parameterization for PAR because there are parameters, such for example Total Ozone Column (TOC) and the Columnar Water Vapor (TCWV), that affect significantly only UV (the former) or VIS (the latter) wavelengths. The range of parameters for which the LUTs were created is shown in Table 1.

 doi:10.20944/preprints202404.0431.v1

Table 1. Range of parameters for which the two LUTs were created.

Parameter	Range for UVI, VID, DNA, PLG, PLD	Range for PAR
Aerosol Optical Depth (AOD) at 550 nm	0 – 2, step = 0.1	0 – 2, step = 0.05
Angstrom Exponent (AE)	0.4 – 2, step = 0.4	0.4 – 2, step = 0.4
Single Scattering Albedo (SSA)	0.6 – 1, step = 0.1	0.6 – 1, step = 0.1
Solar Zenith Angle (SZA)	1° – 89°, step = 2°	1° – 89°, step = 1°
Total Ozone Column (TOC)	200 – 600 DU, step = 10 DU	200 – 500 DU, step = 100 DU
Columnar Water Vapor (TCWV)	2 cm	0.5 – 3 cm, step = 0.5 cm
Surface Albedo	0.05	0.2

The LUTs for UVI, VID, DNA, PLG and PLD were generated using a common LUT that encompassed global surface solar spectral irradiance within the wavelength range of 290 – 400 nm, with a 0.5 nm increment. The solar spectra were multiplied with the effective spectra for erythema [59], for the production of vitamin D in the human skin [28], for the UV-induced DNA damage [60,61], for plant growth [62] and plant damage [63], respectively, and subsequently they were integrated over the 290 – 400 nm interval. In contrast, the LUT for PAR was developed from a separate LUT that included spectra within the broader range of 280 – 3000 nm, with a 1 nm increment. The irradiance within the range of 400 – 700 nm was integrated to obtain the PAR LUT. A correction for the variations of the extraterrestrial solar radiation due to the changes in Earth – Sun distance was also applied.

To create the spectral LUTs, the UVSPEC model from the libRadtran package [64,65] was employed. The foundational model settings were consistent for both spectral LUTs used in the calculations for UVI, VID, and PAR, and these settings are detailed in Table 2.

Table 2. UVSPEC settings for the creation of the LUTs.

Parameter	libRadtran settings
Number of streams	6
Solver	sdisort [66]
Molecular absorption parameterization	reptran coarse [67]
Atmospheric profile	Standard US atmosphere [68]
Extraterrestrial solar spectrum	Kurucz [69]
Aerosol profile	Settle (1990) [70]

Initially, clear-sky radiometric quantities were computed at a spatial resolution of 0.4°x0.4° through the application of linear interpolation across multiple dimensions of the Look-Up Tables (LUTs) corresponding to the following parameters: Aerosol Optical Depth at 550 nm (AOD550), Angstrom Exponent (AE), Single Scattering Albedo (SSA), Total Ozone Column (TOC), and Columnar Water Vapor (TCWV). Detailed information on these parameters can be found in Table 3. AOD550, AE, and TCWV are provided at a temporal resolution of 3 hours, while TOC is available daily and SSA is provided on a monthly basis. In cases where TOC data is unavailable for a specific day, climatological values are used as a substitute. Subsequently, the clear-sky derived irradiances were interpolated to a final resolution of 0.05°x0.05°. This interpolation involved applying a correction for the effect of height on solar radiation and the cloud modification factor (CMF) to retrieve the quantities under all-sky conditions. UV quantities were assumed to increase by 5% per kilometer, while PAR was assumed to increase by 2% per kilometer, similarly as in previous studies [54,71]. The CMF was calculated as the ratio between the all-sky irradiance [72] and the clear-sky irradiance [73], from the CAMS Solar radiation service. This is basically the output of the McCloud model described in the study by Qu et al. [72], which is also called clear sky index and describes the

 doi:10.20944/preprints202404.0431.v1

extinction of solar irradiance by clouds, which is calculated based on input from Meteosat Second Generation (MSG) satellites. Then, the CMF for UV (UV_CMF) was calculated from CMF using the methodology suggested by Staiger et al. [74].

Table 3. Parameters utilized for constructing the climatology of radiometric quantities.

Parameter	Source	Spatial resolution	Temporal resolution	Main reference
AOD550, AE, TCWV	CAMS global reanalysis (EAC4)	0.75x0.75 degrees	3 hours	[75]
SSA	MACv3 aerosol climatology	0.4x0.4 degrees	Monthly	[76]
TOC	OMI AURA Level 3	0.25x0.25	Daily	[77]
CMF	CAMS solar radiation	0.05x0.05	15-min	[72]

The PAR and the effective UV doses are expressed in units of watts per square meter (W/m^2). PAR, which represents the integral of irradiance within the 400 to 700 nm wavelength range, is traditionally quantified in terms of the number of photons received by a surface over a specified duration, known as Photosynthetic Photon Flux Density (PPFD) [78]. PPFD is typically measured in units of micromoles per square meter per second ($\mu mol \cdot m^{-2} \cdot s^{-1}$). To convert PAR from W/m^2 to PPFD, a commonly used conversion factor of 4.57 $\mu mol\ m^{-2}\ s^{-1}$ is applied [79]. In the context of plant growth and morphology, characterizing light availability for plants is often done through the concept of the Daily Light Integral (DLI) [80]. DLI represents the daily flux of photons per unit ground area and takes into account both diurnal variations in light intensity and variations in day length, hence it provides a more comprehensive assessment of light exposure for plants throughout a day. In this manuscript, the term DLI is used interchangeably with PAR.

2.2. Ground-Based and Satellite Datasets

For the evaluation of the model outputs comparisons with satellite-derived products were performed.

Specifically, for PAR, we utilized the SARAH edition 3.0 dataset from the EUMETSAT Climate Monitoring Satellite Application Facility (CM-SAF) [81]. This dataset offers instantaneous values at 30-minute intervals in a spatial resolution of 0.05°x0.05°, expressed in $\mu mol\ m^{-2}\ s^{-1}$. Daylight integrals were computed using the described methodology, akin to that applied for the model outputs. The spectral information, crucial for accurate PAR assessment, is derived using the SPECMAGIC clear-sky model with daily water vapor and ozone information from ERA-5, MODIS-based surface albedo, and MACC-based monthly climatological aerosol information. This model employs the irradiance values across the Kato bands, and the visible is used for the PAR calculation under cloud-free conditions [82]. The effective cloud albedo, derived directly from MSG satellite data based on a modified Heliosat method, is used to account for the influence of clouds on surface irradiance. The efficacy of PAR estimations from the CM-SAF SARAH-3.0 dataset has been validated against ground-based measurements from various stations, exhibiting excellent correlation ($R > 0.95$) and an average mean error bias across all stations and weather conditions of less than 10% [12].

The Tropospheric Emission Monitoring Internet Service (TEMIS), operational since 2001 under the auspices of the European Space Agency (ESA) and the Royal Netherlands Meteorological Institute (KNMI) delivers near-real-time UV radiation data through its online platform (www.temis.nl/uvradiation/uVdose.html; version 2.0; [83]. Tailored for environmental and public health research, TEMIS UV offerings include the clear-sky noon UV index alongside daily doses for three key health-related UV products: Erythemal UV, Vitamin D synthesis, and generalized DNA-damage. The UV-CMF, on which the TEMIS UV processing is based, is determined from cloud observations by the MSG satellites. The data are provided on a 0.25°×0.25° (longitude × latitude) grid with each grid cell covering an area of approximately 28 km (north–south) × 17 km (east–west), both

 doi:10.20944/preprints202404.0431.v1

for clear-sky and all-sky conditions. The daily integrals are given in kJ/m^2. Detailed methodologies behind these products are discussed in [71].

Ground-based measurements of global horizontal irradiance (GHI), collected from the meteorological service network of Cyprus at stations located in Agros, Larnaka, and Athalassa, served as benchmarks to evaluate the model's proficiency in capturing diurnal cloud variations.

2.3. Statistical Metrics

To assess the accuracy and reliability of the model, various statistical metrics were employed. These include the Mean Absolute Error (MAE), which measures the average magnitude of the errors in a set of predictions; the Median, representing the midpoint of the data set's error distribution; the Root Mean Square Error (RMSE), providing a measure of the differences between values predicted by the model and the values observed; the Interquartile Range (IQR), which evaluates the variability in the middle 50% of the dataset; and the Standard Deviation (STD), which quantifies the dispersion of the dataset from the mean.

The determination of trends in the dataset utilized a straightforward linear regression model applied on a seasonal basis. To ascertain the statistical significance of the observed trends, the p-value was calculated using the Wald Test with a t-distribution for the test statistic [84]. A p-value below the threshold of 0.05 indicated that the trend was statistically significant at the 95% confidence level, leading to the rejection of the null hypothesis that posits a slope of zero.

3. Results and Discussion

3.1. Comparison of Model against Satellite and Ground-Based Measurements

In this section, we compare the radiometric quantities derived from the model with those obtained from other, well established, satellite-based sources. Additionally, we evaluate the model's ability to accurately represent the daily variations in the cloud cycle, using ground-based derived CMF as a benchmark.

3.1.1. Evaluation of Effective UV Products

Figure 1 provides a comparative analysis of the modeled daily erythemal UV doses against the daily UV doses from TEMIS. The scatter plot reveals a robust linear relationship, as indicated by the high correlation coefficient (R^2 = 0.96). This strong correlation demonstrates the good agreement between the TEMIS data and the model. The histogram on the right shows that the differences between the model and TEMIS values are almost symmetrically distributed around zero.

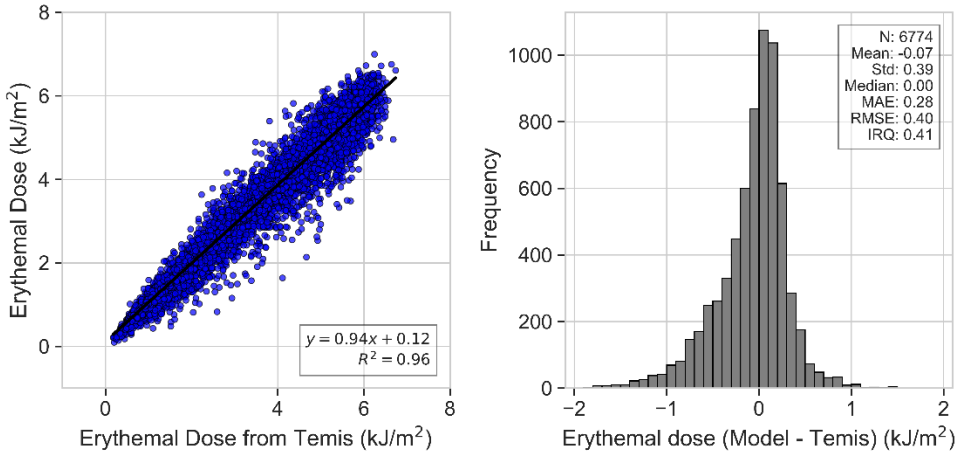

Figure 1. Scatter plot between the daily erythemal UV doses from the model and TEMIS (left panel). Distribution of the absolute differences between daily erythemal doses from the model and TEMIS (right panel).

 doi:10.20944/preprints202404.0431.v1

Figure 2 presents a comparative analysis of daily UV Cloud Modification Factors (UV-CMF) from the model and those retrieved from the TEMIS, against the daily UV-CMF that has been calculated by ground-based GHI measurements. The UV-CMF is computed by dividing the integrated daily erythemal UV dose under all-sky conditions by that under the same atmospheric conditions, but without clouds. Since reliable measurements of the erythemal UV doses were not available, we calculated the UV-CMF from the GHI measurements with a 15 min step using the methodology of [74], and then multiplied with the corresponding clear-sky modelled UV doses. The daily dose under all-sky conditions was then calculated by integrating the calculated values for each day. The corresponding clear-sky daily integrals were calculated from the modelled erythemal UV doses. The effect of clouds (as derived from the GHI measurements) on the daily erythemal doses (i.e., the daily UV-CMF) was finally calculated by dividing the all-sky with the clear-sky daily UV doses. The scatter plots (a and b) display a strong linear relationship between the measured UV-CMF and those estimated by both the model and TEMIS, with high correlation coefficients (R^2 values of 0.89 and 0.90, respectively), indicating robust power in estimating daily erythemal UV dose and agreement with the ground-based measurements.

The bottom panels (c and d) show the frequency distribution of the differences between the measured and the estimated UV-CMF values for the model and TEMIS, respectively. The centered distributions near zero suggest a good agreement overall, with minimal bias in the central tendency as indicated by the mean difference close to zero. Moreover, the similar shapes and spread of the distributions, evidenced by the standard deviation and interquartile range, confirm the consistency of the estimations. This comparative assessment highlights the efficacy of the model in capturing the variability of UV exposure due to cloud cover.

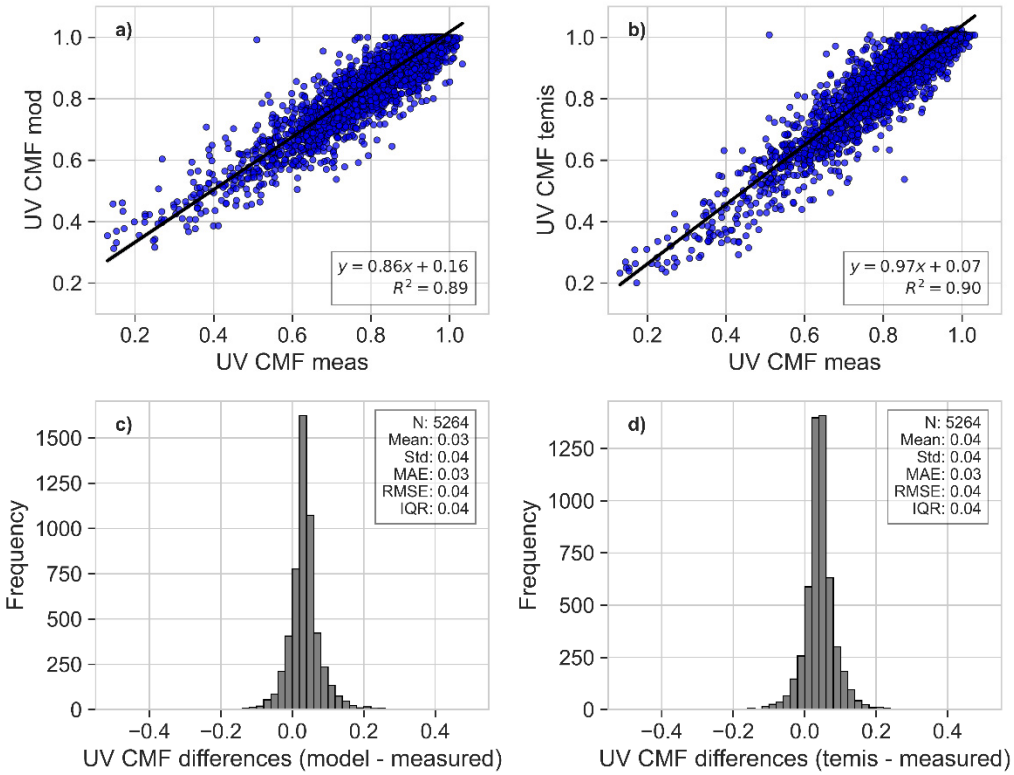

Figure 2. Scatter plot between a) daily erythemal UV CMF from the model and the ground-based measurements, b) daily erythemal UV CMF from TEMIS and the ground-based measurements. Distribution of the absolute differences between c) Erythemal UV CMF from the model and measurements and d) TEMIS and measurements.

 doi:10.20944/preprints202404.0431.v1

3.1.2. Evaluation of PAR

Figure 3 provides a comparison of the DLI obtained from a model against the DLI from the CM-SAF SARAH-3 dataset. The strong linear relationship in the scatter plot is evidenced by a high coefficient of determination ($R^2 = 0.97$), indicating excellent agreement between the two datasets. The histogram on the right details the distribution of differences between the model's DLI and CM-SAF's DLI, centered very close to zero with a mean of -0.06 mol m^{-2} day^{-1}, suggesting a negligible systematic bias. The spread of the differences, reflected in the standard deviation of 2.73 mol m^{-2} day^{-1}, and interquartile range (IQR) of 3.33 mol m^{-2} day^{-1}, indicate the variability in the data comparison.

This comparison demonstrates the model's robustness in estimating the DLI, capturing the essence of day-to-day variability with a high degree of precision.

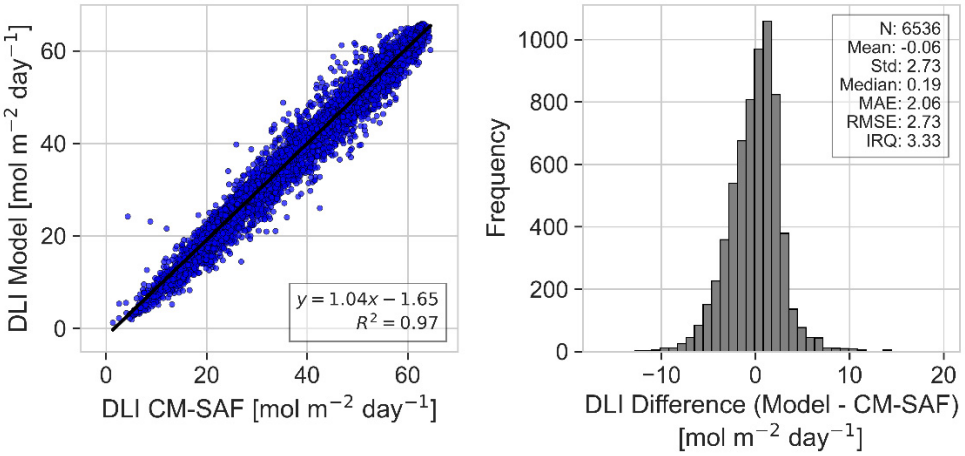

Figure 3. Scatter plot between the DLI from the model and CM-SAF SARAH-3 (left panel). Distribution of the absolute differences between DLI from the model and CM-SAF SARAH-3 (right panel).

Figure 4 presents a side-by-side comparison of Photosynthetically Active Radiation Cloud Modification Factor (PAR CMF) estimates from the model and the CM-SAF dataset against measured values. The daily PAR CMFs for the model and CM-SAF datasets were calculated from the daily integrals divided with the corresponding clear-sky integrals obtained from the model. Panels (a) and (b) depict scatter plots showing the linear regressions of model-estimated and CM-SAF PAR CMF against the measured values, with corresponding R^2 values of 0.88 and 0.77, respectively. The model demonstrates a stronger correlation with the measured data, suggesting it may offer a more accurate representation of PAR CMF under varying sky conditions.

The histograms in panels (c) and (d) display the distributions of the differences between the model/CM-SAF estimates and the measured values. Both distributions are centered around zero, with the model having a slight skewness towards positive values. However, the model exhibits a tighter distribution with a standard deviation and interquartile range (IQR) of 0.07, compared to the CM-SAF's 0.08, reflecting slightly higher precision in the model's estimates. The mean absolute error (MAE) and root mean square error (RMSE) further corroborate this, being lower for the model's estimates (0.04 and 0.06, respectively) than for CM-SAF's (0.05 and 0.07, respectively).

 doi:10.20944/preprints202404.0431.v1

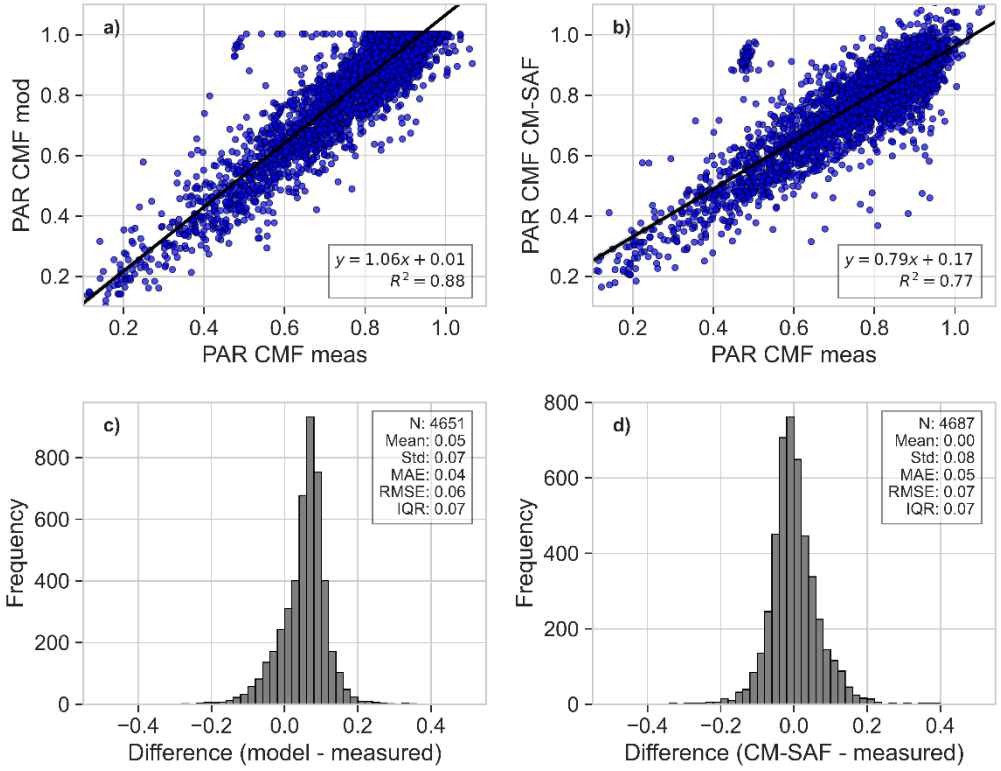

Figure 4. Scatter plot between a) daily PAR CMF from the model and the ground-based measurements, b) daily PAR CMF from CM-SAF and the ground-based measurements. Distribution of the absolute differences between c) PAR CMF from the model and measurements and d) CM-SAF and measurements.

3.2. PAR and UV Climatology and Trends

In section 3.2.1, we delve into the seasonal climatologies and the annual cycles of DLI and noon UVI, providing a detailed examination of their variations and impacts across different times of the year. This analysis is crucial for understanding the temporal dynamics of solar radiation and its effects on both ecological systems and human health. The comprehensive discussions in this section are complemented by graphical representations, which elucidate the patterns and trends observed in our data. For additional insights into the effects of UV solar radiation, including the dose of vitamin D, DNA damage potential, as well as plant growth and damage, we have included detailed figures in Appendix A. These figures extend our analysis to encompass a broader spectrum of solar radiation impacts, offering a complete overview of its multifaceted roles.

In section 3.2.2, we conduct a trend analysis focused on DLI and noon UVI. Given that the trends observed in noon UVI are representative of the patterns seen in the other effective UV quantities (vitamin D dose, DNA damage, plant growth, and plant damage), we have chosen to concentrate our discussion on DLI and UVI.

3.2.1. Climatology

The mean seasonal noon UVI across Cyprus is shown in the appendix at Figure A1. UVI values are represented through a color-coded scale, indicating intensities from low to high, with blue representing lower values and red representing higher values. Since, from the overall means is quite difficult to depict any spatial variations, we will discuss them with respect to the relative spatial variations from the overall seasonal mean, which is given in Table 4.

Preprints.org (www.preprints.org) | NOT PEER-REVIEWED | Posted: 5 April 2024 doi:10.20944/preprints202404.0431.v1

Table 4. Overall mean seasonal noon UVI and DLI, along with the respective standard deviations.

Season	Mean noon UVI	Standard Deviation of mean noon UVI	Mean DLI (mol m^{-2} day^{-1})	Standard Deviation of mean DLI (mol m^{-2} day^{-1})
Winter	2.6	0.18	21.9	1.02
Spring	7.0	0.24	47.8	0.98
Summer	9.5	0.24	61.4	1.12
Autumn	5.0	0.21	36.1	0.95

Figure 5 provides a detailed representation of the relative spatial UVI anomalies across Cyprus, reflecting the deviations from the seasonal mean in percentage terms. The latitudinal pattern observed, with northern areas exhibiting lower UVI values and southern areas higher, aligns with expectations given the variations in solar elevation angle throughout the seasons.

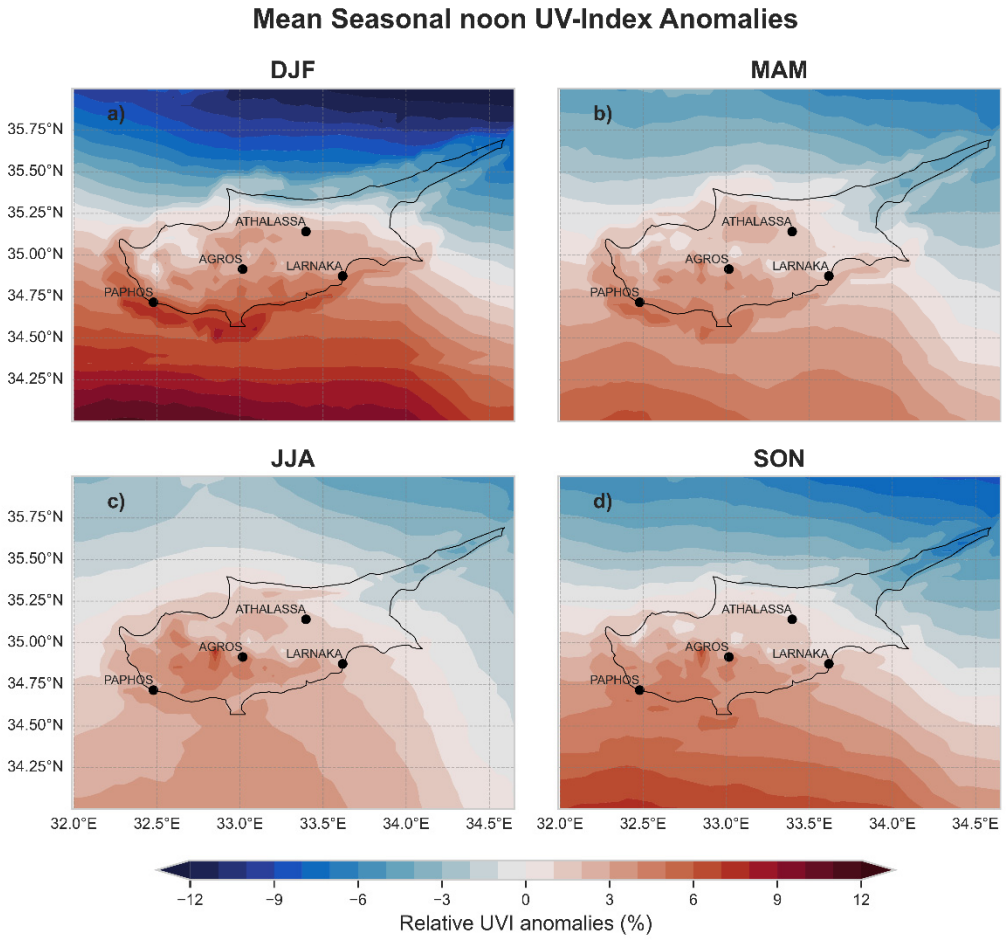

Figure 5. Relative seasonal noon UVI anomalies over Cyprus.

Winter displays the more pronounced latitudinal gradient. During winter, the solar elevation is at its lowest, enhancing the latitudinal effect. This is evidenced by the larger standard deviation of the mean UVI values, which indicates a wider spread in the data. In contrast, during summer, the high solar elevation reduces the latitudinal impact on UVI deviations, coinciding with the least variability in UVI values.

The transitional seasons of spring and autumn provide insightful transitions in UVI variability. During spring, the increasing solar elevation begins to lessen the latitudinal gradient observed in winter, while autumn sees a return to greater variability as the solar elevation decreases. These

 doi:10.20944/preprints202404.0431.v1

seasons may also see the influence of changing weather patterns, such as the development or recession of the Mediterranean sea breeze, which can differentially impact coastal and inland regions.

Apart from the clear latitudinal influence, topographical features play a significant role in shaping UVI distribution. The anomalies over coastal regions show higher values compared to the biggest part of the inland, showing that there are different changes in different regions.

The UVI anomalies are not only a reflection of latitudinal and topographical influences but also of atmospheric conditions such as aerosol load, cloud cover, and ozone concentration. For instance, areas with increased aerosol presence can experience reduced UVI due to the scattering and absorption of UV radiation. The influence of such atmospheric components may help explain some of the spatial variations observed, particularly in areas where the deviations from the mean are not readily explained by latitude or topology alone.

To further examine these factors, we analyze the annual cycle of noon Ultraviolet Index (UVI) values for three distinct locations within Cyprus, each representing different environmental conditions: Agros (inland, high altitude), Athalassa (inland, middle altitude), and Larnaka (coastal, low altitude). Figure 6 illustrates the mean UVI values over the months, alongside the standard deviation, which indicates the variability in these values. From the annual cycle graph, we observe that all three sites follow the typical bell-shaped curve expected with seasonal solar elevation changes. However, the nuances in the data reveal the influence of topography and altitude. Agros, with its high altitude, experiences the most intense UVI, particularly during the months when solar elevation is highest, confirming the trend that UV radiation increases with altitude due to the thinner atmospheric layer filtering the UV rays.

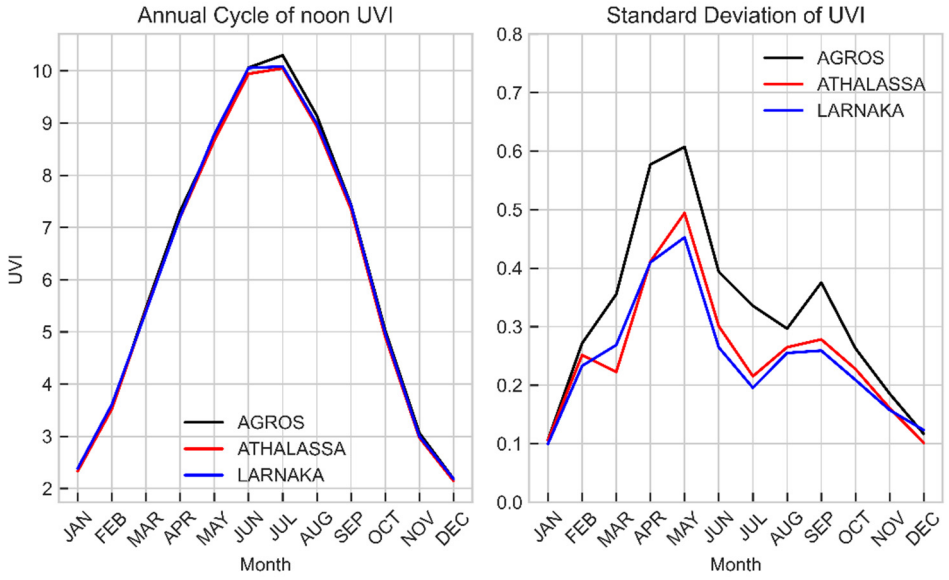

Figure 6. Monthly average noon UVI for the period 2004 – 2023 for Agros, Athalassa, and Larnaka (left panel), and the corresponding standard deviation (right panel).

The standard deviation graph shows a pronounced spike in the spring months across all sites, with the most considerable variability occurring at Agros. This variability can be attributed to transient weather patterns that include fluctuating cloud cover and the intrinsic variability in total ozone concentration during spring. Additionally, spring is characterized by intense dust events originating either from North Africa or Middle East [85,86], which is also contributing to the observed variability. Total ozone columns values are also maximum during spring, while at this season it has its highest variability. The higher total ozone values in spring also justify why for example the average noon UVI in May is lower than the average noon UVI in August despite the larger SZAs in May. May and the summer months are noteworthy for reaching very high to extreme (10+) UVI values, accentuated at higher altitudes as seen at the Agros site. Despite the high altitude of Agros

Preprints.org (www.preprints.org) | NOT PEER-REVIEWED | Posted: 5 April 2024 doi:10.20944/preprints202404.0431.v1

providing slightly higher UVI readings, the overall differences among the sites remain minimal. This can be seen in both Figures 5 and 6, suggesting a relative uniformity in UVI exposure across Cyprus. This uniformity across diverse topographical and geographical regions emphasizes the pervasive nature of UV radiation and the importance of sun safety measures regardless of specific location within the region.

The seasonally averaged daily DLI is shown in Figure A2 at Appendix, with the seasonal mean values can be seen in Table 4. Figure 7 presents the relative DLI spatial anomalies from the overall mean for each season. Throughout the year, the DLI is generally lower over higher altitudes relative to lower altitude areas, which can primarily be attributed to the increased cloud attenuation experiences at higher elevations. The spatial variability observed in DLI is more pronounced relative to the one seen in the UVI, mainly for three reasons: (1) altitudinal effects on UV are more significant compared to visible solar radiation (i.e., UV increases faster with altitude relative to the PAR), (2) cloud have a more substantial impact on PAR than on UV radiation, 3) DLI is the cumulative measure of PAR over the course of a day, thereby encompassing all variations in cloud cover during daylight hours. In contrast, UVI is measured around local noon and only reflects cloud presence at that specific time. This temporal aspect means that DLI captures a broader scope of cloudiness, whereas UVI may not be as sensitive to changes in cloud cover outside of midday. Thus, the effects of altitude and clouds are cancelled out for the UVI. Seasonally, the average DLI varies considerably, with values ranging from ~ 20 mol m^{-2} day^{-1} in the winter months to ~ 60 mol m^{-2} day^{-1} during the summer.

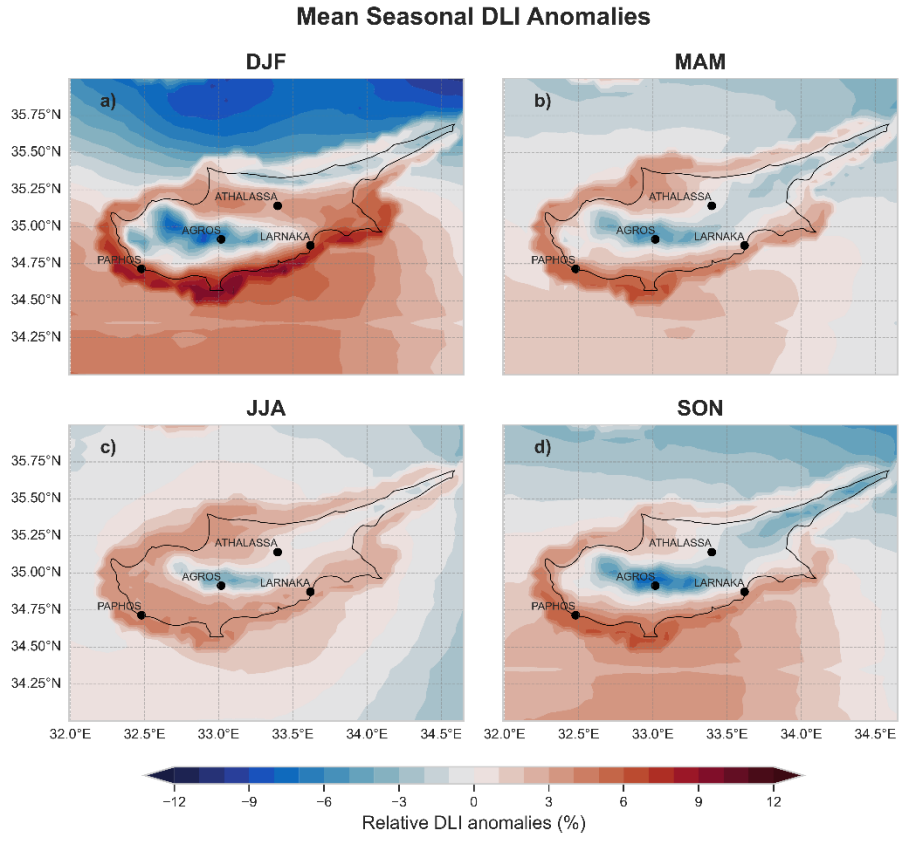

Figure 7. Relative seasonal DLI anomalies over Cyprus.

Contrary to the UV outcomes, we observe that the DLI is generally lower over Agros, a higher-altitude site, compared to the two lower-altitude locations (Larnaka and Athalassa) (Figure 8). As explained above, this is mainly due to the prevalence of clouds, which have a more pronounced effect on DLI over the effect of altitude. The DLI at Agros ranges from 20 mol m^{-2} day^{-1} in the cloudier months of December and January to ~ 65 mol m^{-2} day^{-1} during the clearer skies of June and July (Figure 8). Notably Larnaka, which is a coastal city, exhibits the highest DLI values in June, while

 doi:10.20944/preprints202404.0431.v1

Agros and Athalassa, being further inland, reach their peak DLI in July. The coastal influence likely mitigates cloud cover in June at Larnaka, whereas inland areas like Agros and Athalassa experience a delayed peak in DLI due to more significant cloud effects during this period. Despite higher SZAs and longer days in June, it is the reduced cloudiness in July that results in the maximum DLI observed at the inland sites.

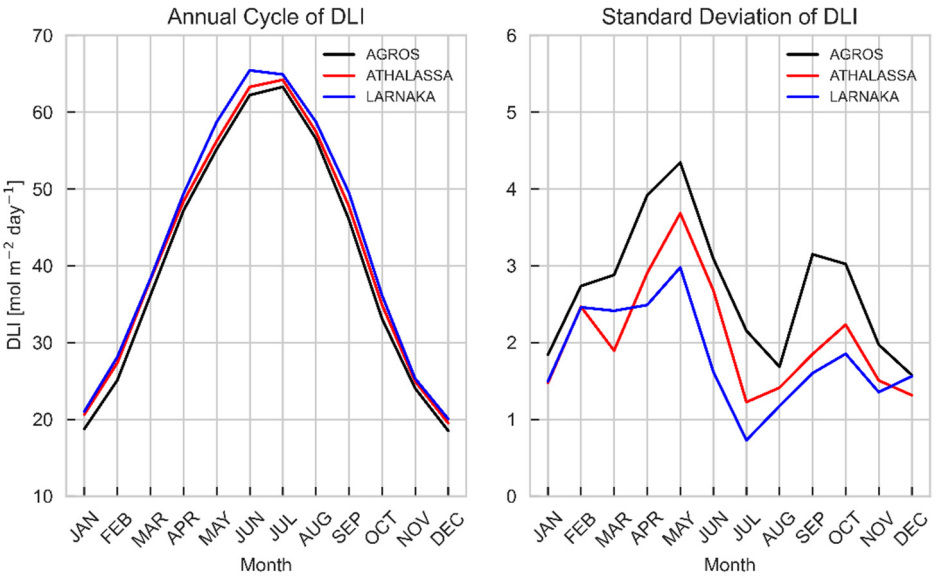

Figure 8. Same as Figure 6 for the monthly average daily DLI.

The effect of clouds on the monthly average noon UVI (left) and DLI (right) are presented in Figure 9. It demonstrates that during winter, cloud attenuation is more pronounced on DLI by about 5-10%, with a reduction of 18-30%, compared to a 15-25% reduction in UVI. Conversely, in summer, the attenuation on both DLI and UVI is comparable and generally low (less than 10%). This reduced impact in summer is due to the typical clearer skies observed in that period of the year over Cyprus. As expected, the higher altitude location of Agros consistently experiences greater cloud-induced attenuation.

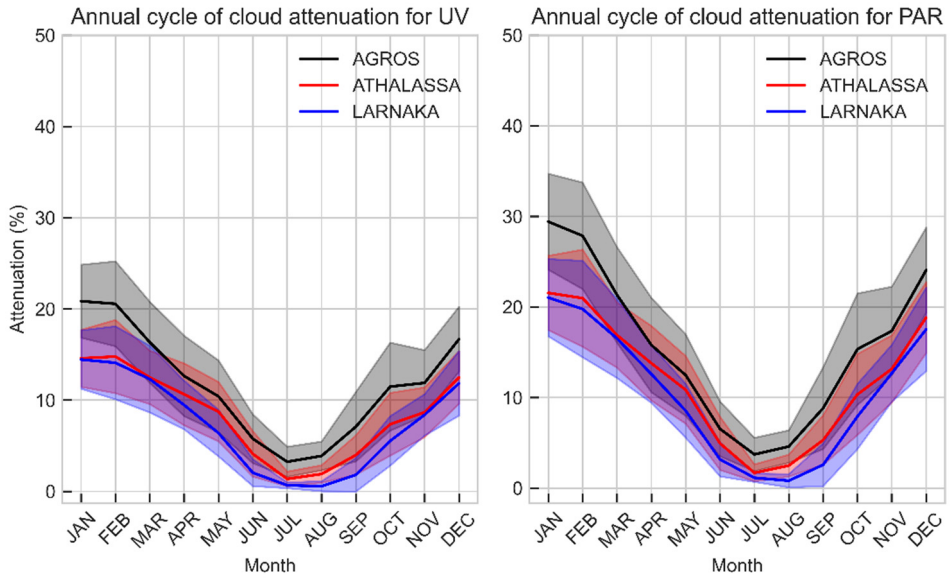

Figure 9. Monthly average attenuation of the daily average UVI (left) and daily PAR (right) for the period 2004 – 2023 for Agros, Athalassa, and Larnaka. Shaded areas represent the standard deviation range (1σ).

 doi:10.20944/preprints202404.0431.v1

3.2.2. Trends

Figure 10 illustrates the seasonal trends in noon UVI across Cyprus for the years 2004 to 2023, based on the climatology previously discussed. These trends are primarily influenced by variations in cloud cover, aerosol concentrations, and ozone levels. Analysis of the impact of cloud attenuation on seasonal noon UVI, detailed in Figure 12, indicates a marginal yet statistically nonsignificant rise in UVI during most seasons, except for winter (DJF). This increase becomes statistically significant in the summer (JJA) over maritime regions, while changes over terrestrial areas are minimal. It's clear that while cloud cover is influential in determining the overall direction of noon-UVI trends, still they cannot fully explain the UVI trends, thus changes in AOD and TOC also play substantial roles in the observed variations.

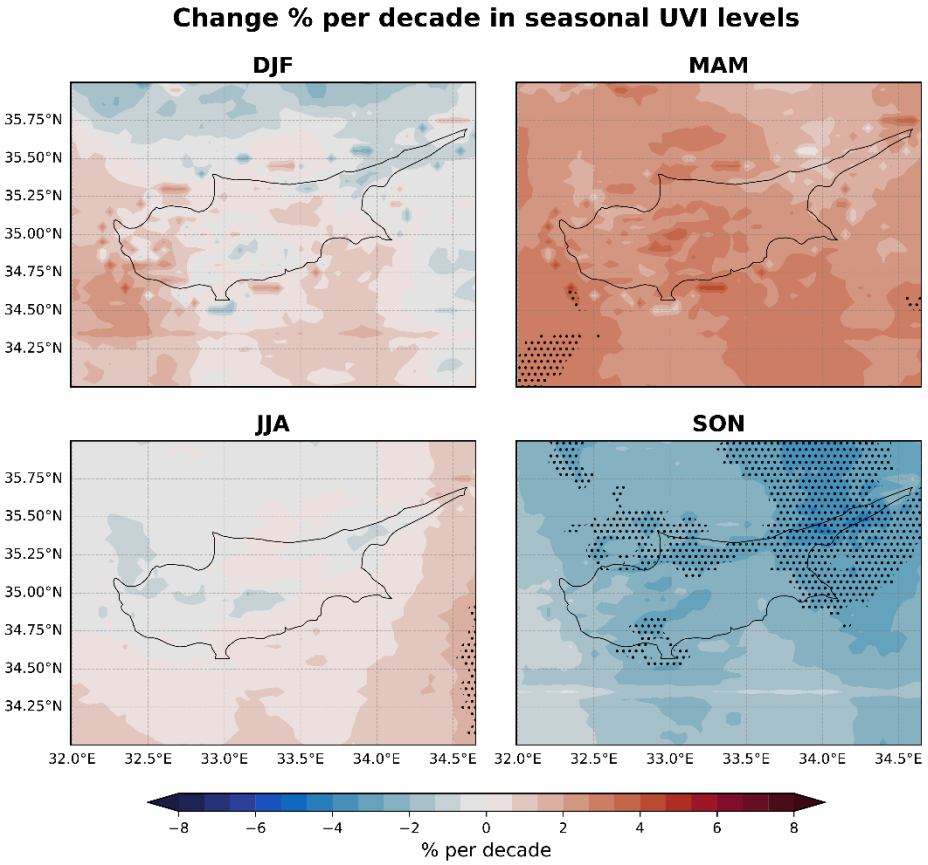

Figure 10. Trends in the seasonal average noon UVI for the period 2004 – 2023. Statistically significant trends are marked with x.

AOD trends, depicted in Figure 14, generally exhibit a downward trend across all seasons, except for autumn (SON), which shows positive trends. Nonetheless, these variations do not achieve statistical significance. On the other hand, Figure 15 reveals significant declines in TOC during winter and spring (MAM), no notable changes in summer, and significant increases in autumn. Winter reveals notable spatial variability in UVI trends, with certain areas, especially in the south and west, showing slight positive trends, in contrast to the negative trends observed in the north and northeast. Despite this spatial diversity, the trends remain statistically insignificant. The transition seasons—spring and autumn show complex patterns: spring is characterized by positive, though statistically insignificant, UVI trends, while autumn sees significant negative trends in the north and east of the island. This autumnal decrease is mainly attributed to significant positive TOC trends of 2–3% shown in Figure 15, and the nonsignificant positive trends in AOD depicted in Figure 14. Summer showcases a uniformity in UVI levels, indicating a stable pattern of UV exposure during these months, unaffected significantly by changes in clouds or TOC. In summary, the observed shifts in UVI

 doi:10.20944/preprints202404.0431.v1

throughout the year suggest a nuanced interplay between cloud cover, aerosols, and ozone levels, with each factor contributing differently across seasons and regions. The significant seasonal and spatial variations underscore the importance of considering multiple atmospheric factors when assessing UVI trends.

Figure 11 shows the seasonal trends in DLI across Cyprus. These trends exhibit some correspondence with UVI patterns, yet they manifest with subtler intensity, underscoring the differential sensitivity of DLI to atmospheric conditions. Considering that ozone selectively absorbs ultraviolet light with minimal impact on the visible spectrum, the fluctuations in DLI are primarily governed by cloud cover and aerosols rather than ozone alterations.

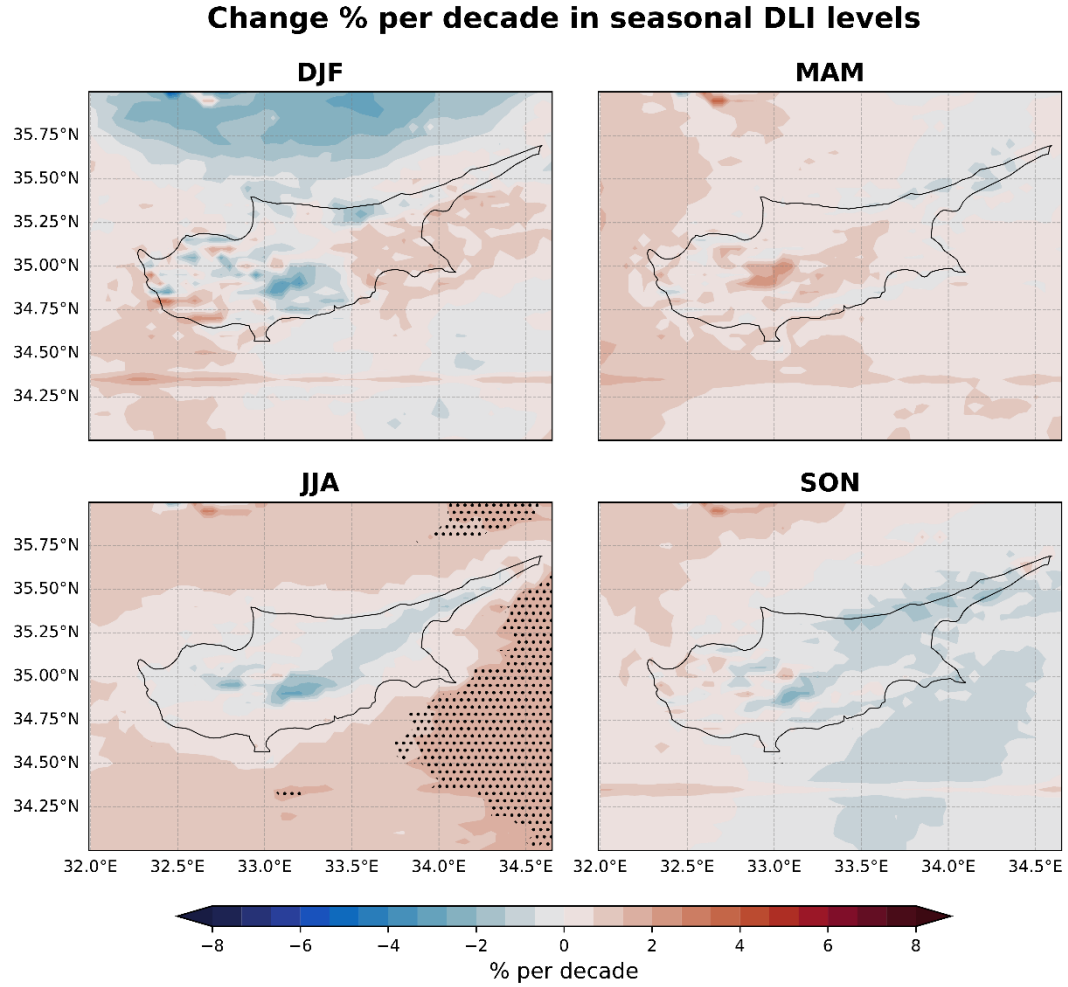

Figure 11. Trends in the seasonal average daily DLI for the period 2004 – 2023. Statistically significant trends are marked with x.

In the winter, DLI exhibits a mosaic of trends, reflecting a nuanced interplay with cloud attenuation patterns (Figure 13) observed alongside UVI trends. The variation in DLI, especially in the magnitude of change, could be attributed to two principal factors: (a) the negligible influence of ozone on visible light, and (b) the comprehensive temporal scope of DLI measurements encompassing the entire daylight period as opposed to the singular midday UVI recordings. This disparity suggests that cloud cover, or its optical properties, may fluctuate differently throughout the day, creating distinct signatures in UVI and DLI datasets.

Preprints.org (www.preprints.org) | NOT PEER-REVIEWED | Posted: 5 April 2024 doi:10.20944/preprints202404.0431.v1

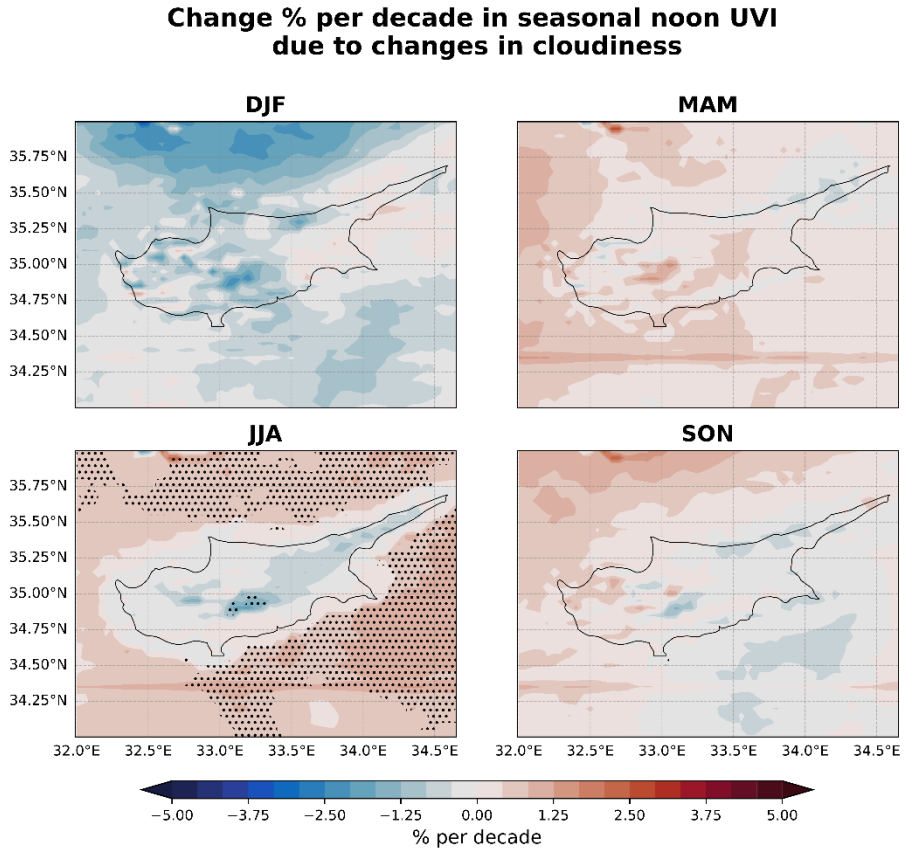

Figure 12. Trends in the seasonal noon UVI (in %) due to attenuation by clouds for the period 2004 – 2023. Statistically significant trends are marked with x.

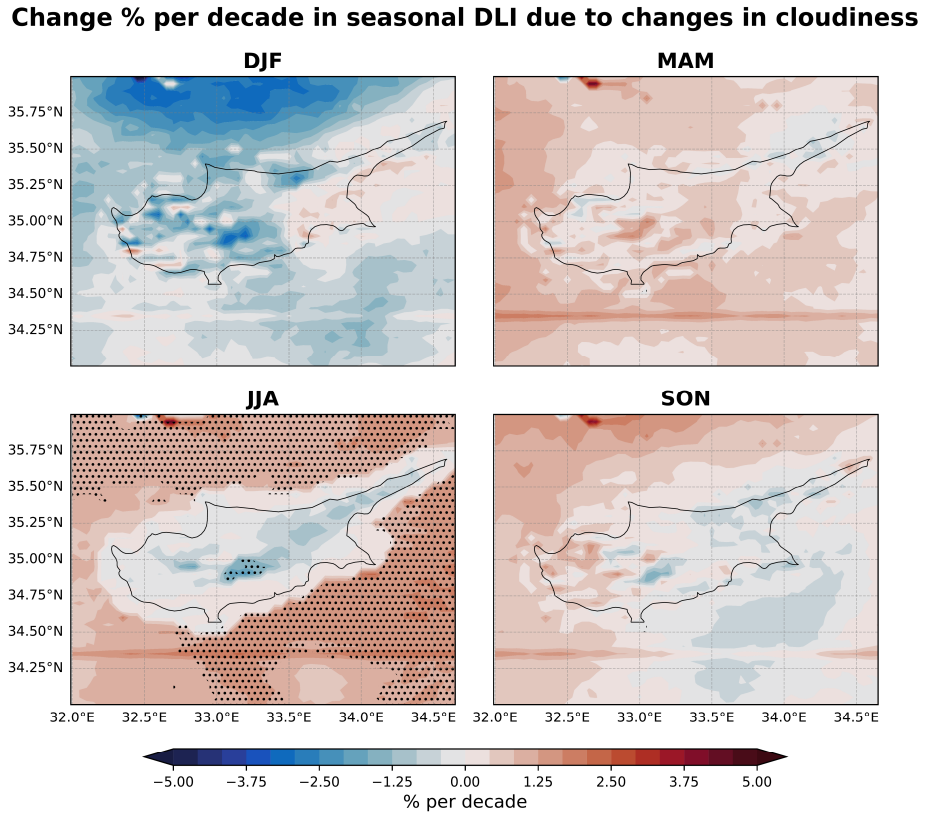

Figure 13. Same as Figure 12 but for DLI.

Preprints.org (www.preprints.org) | NOT PEER-REVIEWED | Posted: 5 April 2024 doi:10.20944/preprints202404.0431.v1

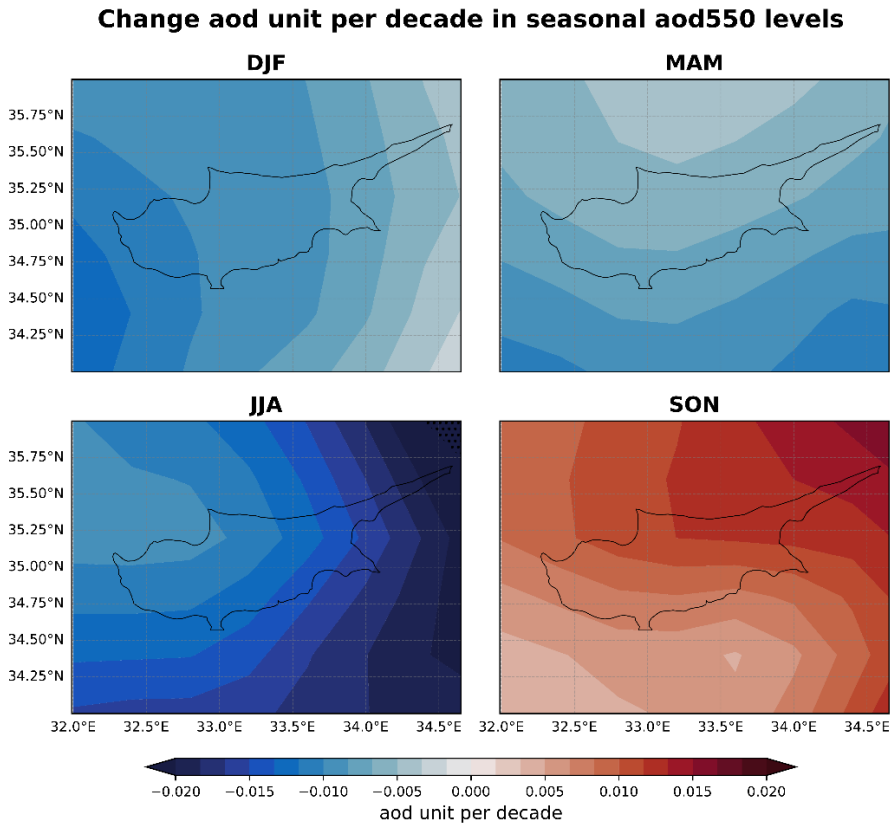

Figure 14. Trends in the seasonal AOD level for the period 2004 – 2023. Statistically significant trends are marked with x.

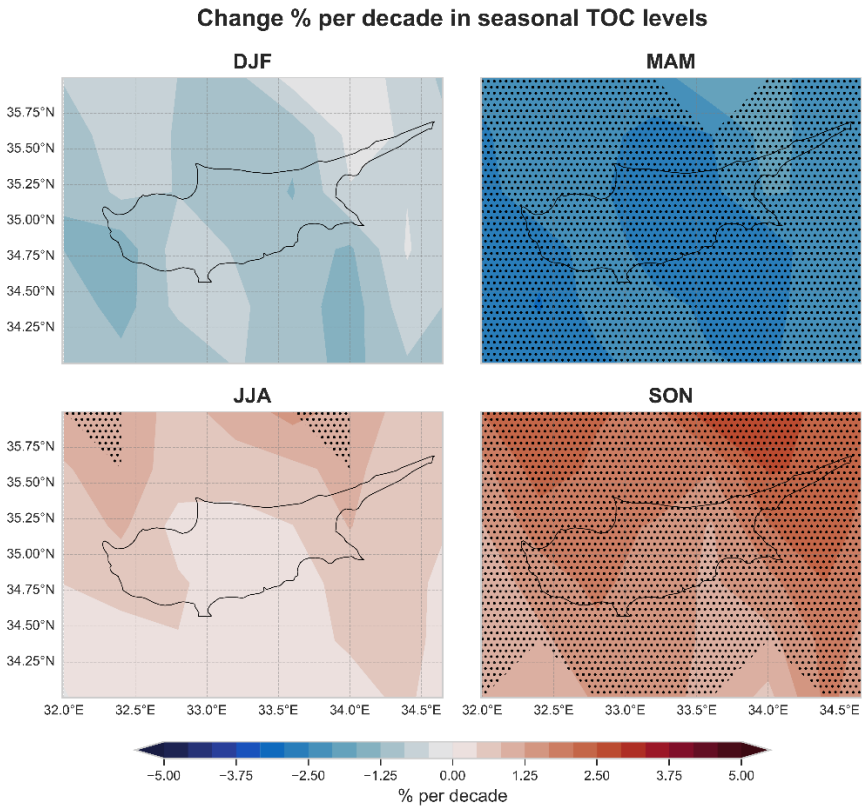

Figure 15. Trends in the seasonal TOC levels for the period 2004 – 2023. Statistically significant trends are marked with x.

 doi:10.20944/preprints202404.0431.v1

During spring DLI trends are influenced by the decline in AOD levels, with cloud cover likely playing a more localized and varied role. The modestly positive DLI trends in the summer across mainland regions, bordering on the neutral, with isolated areas exhibiting minor decreases, suggest stable yet spatially and temporally heterogeneous cloud and aerosol conditions which introduce slight alterations to the visible light spectrum.

Autumn reveals a complex pattern for DLI, contrasting with the more uniform and statistically significant positivity noted in UVI trends. DLI trends are almost neutral with pockets of negative trends dispersed across the region. This contrast underscores the distinct influences that atmospheric components exert on UVI versus DLI. The marginal impact of ozone on DLI underscores this distinction, positing that while significant increases in ozone can modulate ultraviolet radiation, it does not exert a parallel effect on visible light illuminance.

While the study reveals intricate seasonal dynamics influencing UVI and DLI levels, such as cloud cover, aerosol presence, and TOC, the statistical significance of these factors is not uniformly observed across the seasons. This highlights the complexity of environmental interactions that govern solar ultraviolet and visible radiation reception at the Earth's surface.

4. Summary and Conclusions

The study has presented a high-temporal (15-min) and -spatial resolution (0.05˚x0.05˚) climatology for Cyprus, integrating satellite and reanalysis products into a radiative transfer model to generate agriculture and health-related outputs like PAR, Erythemal UV, Vitamin D, DNA damage, plant growth and damage effective UV doses from 2004 to 2023. The new products were found to be consistent with other satellite-based climatological datasets, while ground-based observations have been utilized to further assess the model's fidelity in capturing daily cloud dynamics. More specifically, the UV modeled quantities exhibited a strong correlation with TEMIS data for daily erythemal UV doses and DLI with CMSAF SARAH-3 denoted by correlation coefficients (R^2) of 0.96, and 0.97, respectively.

Analyzing the seasonal spatial variability of UVI, a consistent latitudinal gradient was observed in its distribution across Cyprus, highlighting a stronger influence of solar elevation angles on UVI variability during the winter and autumn seasons. Despite significant seasonal fluctuations driven by solar elevation and atmospheric conditions, differences in UVI among various topographical regions remained remarkably minimal. This finding suggests a relative uniformity in UVI exposure across the region, reinforcing the importance of universal sun safety measures.

The study further revealed that DLI variability is more pronounced than that of UVI, primarily due to its cumulative nature and heightened sensitivity to cloud cover throughout the day. A marked decrease in DLI was noted over higher altitudes, attributed to increased cloud attenuation. This pronounced effect of clouds on DLI, as opposed to UVI, calls attention to the distinct roles of atmospheric constituents in modulating different components of solar radiation.

The study's trend analysis elucidated non-significant spatial variability in UVI trends during winter and non-uniform trends in other seasons, indicating localized environmental impacts. The presence of significant positive trends in TOC during autumn affecting UVI levels was also noted, due to the increase in TOC. In contrast, DLI trends showed more substantial seasonal sensitivity, dictated by the interplay of atmospheric factors, with a particular emphasis on cloud influence.

These findings show the complex interplay between geographic, topographical, and atmospheric factors in shaping solar radiation patterns across Cyprus. They highlight the necessity for comprehensive, region-specific assessments of solar radiation for public health advisories and ecological monitoring. Looking forward, the study paves the way for future research to assess the consistency of these patterns over extended periods, factoring in the potential implications of climate change, and to further explore the localized influences of atmospheric dynamics on solar radiation.

Author Contributions: Conceptualization, K.F., I.F. and S.K.; methodology, K.F, I.F., K.P..; software, K.F, I.F and G.C..; validation, K.F., G.C. and I.F.; formal analysis, K.F.; investigation, K.F, I.F.; resources, I.F. K.P, K.F, A.N, G.C.; data curation, K.F, G.C, I.F.; writing—original draft preparation, K.F., I.F.; writing—review and editing,

 doi:10.20944/preprints202404.0431.v1

K.F, I.F, S.K.; visualization, K.F.; supervision, S.K, D.H..; project administration, S.K.; funding acquisition, D.H. All authors have read and agreed to the published version of the manuscript.

Funding: This research was funded by the 'EXCELSIOR': ERATOSTHENES: Excellence Research Centre for Earth Surveillance and Space-Based Monitoring of the Environment H2020 Widespread Teaming project (www.excelsior2020.eu). The 'EXCELSIOR' project has received funding from the European Union's Horizon 2020 research and innovation programme under grant agreement no. 857510, from the Government of the Republic of Cyprus through the Directorate General for the European Programmes, Coordination and Development and the Cyprus University of Technology.

Data Availability Statement: (1) The climatologies for health-related effective quantities (erythemal UV, DNA damage, and Vitamin D production) are accessible on Zenodo: https://doi.org/10.5281/zenodo.10925634. (2) The agricultural-related quantities (Photosynthetically Active Radiation [PAR], plant growth, and plant damage) are available at Zenodo: https://doi.org/10.5281/zenodo.10925857. (3) CAMS global reanalysis (EAC4) and CAMS solar radiation data can be accessed through the Copernicus Atmosphere Monitoring Service (CAMS) atmosphere data store: https://ads.atmosphere.copernicus.eu/cdsapp#!/search?type=dataset. (4) The MACv3 aerosol climatology (2022) is available for download at: ftp://ftp-projects.zmaw.de/aerocom/climatology/MACv3_2022. (5) OMI Aura Ozone Level 3 data (OMDOAO3e) can be found through the NASA Earthdata Portal: https://search.earthdata.nasa.gov/search?q=OMDOAO3e_003. (6) The Surface Radiation Data Set - Heliosat (SARAH) - Edition 3 is available through the Satellite Application Facility on Climate Monitoring (CM SAF): https://wui.cmsaf.eu/safira/action/viewProduktSearch. (7) TEMIS UV Index and UV Dose Operational Data Products are hosted on the TEMIS website: https://www.temis.nl/uvradiation/UVarchive/uvncfiles.php. All other files are available upon request from the corresponding author.

Acknowledgments: The authors would like to thank the personnel and technicians of the Department of Meteorology of Cyprus for maintaining the stations and providing the data of global horizontal irradiance. We also express our appreciation to the EUMETSAT's Satellite Application Facility on Climate Monitoring (CM SAF) for the provision of the SARAH-3 Photosynthetically Active Radiation (PAR) data. Our thanks go to the UV-Index and UV Dose team at the Tropospheric Emission Monitoring Internet Service for providing free access to UV data.

Conflicts of Interest: The authors declare no conflict of interest.

Appendix A

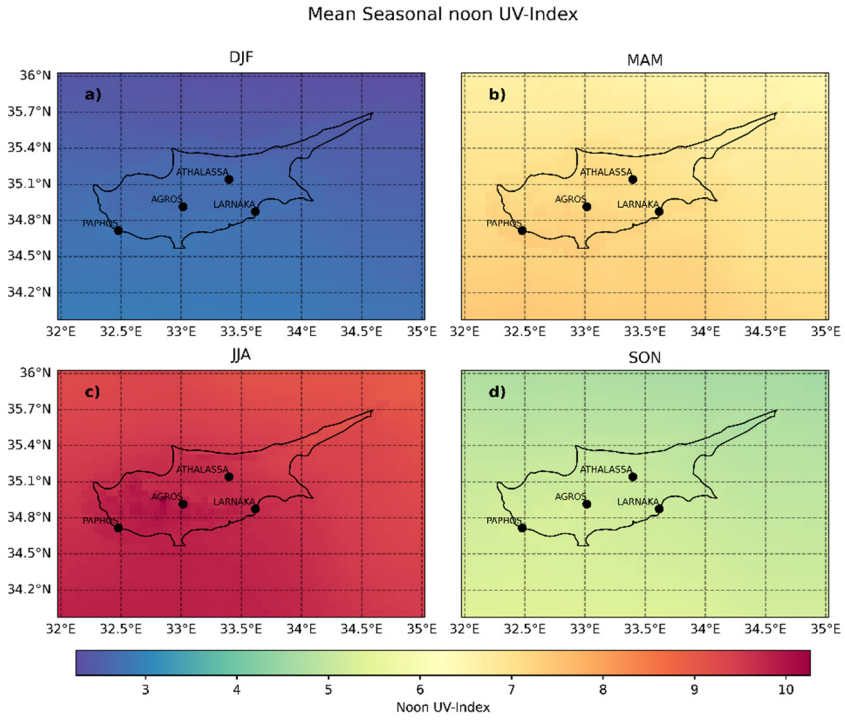

Figure A1. Mean noon UV-Index over Cyprus during the period 2004 – 2023 for a) winter, b) spring, c) summer and d) autumn months.

Preprints.org (www.preprints.org) | NOT PEER-REVIEWED | Posted: 5 April 2024 doi:10.20944/preprints202404.0431.v1

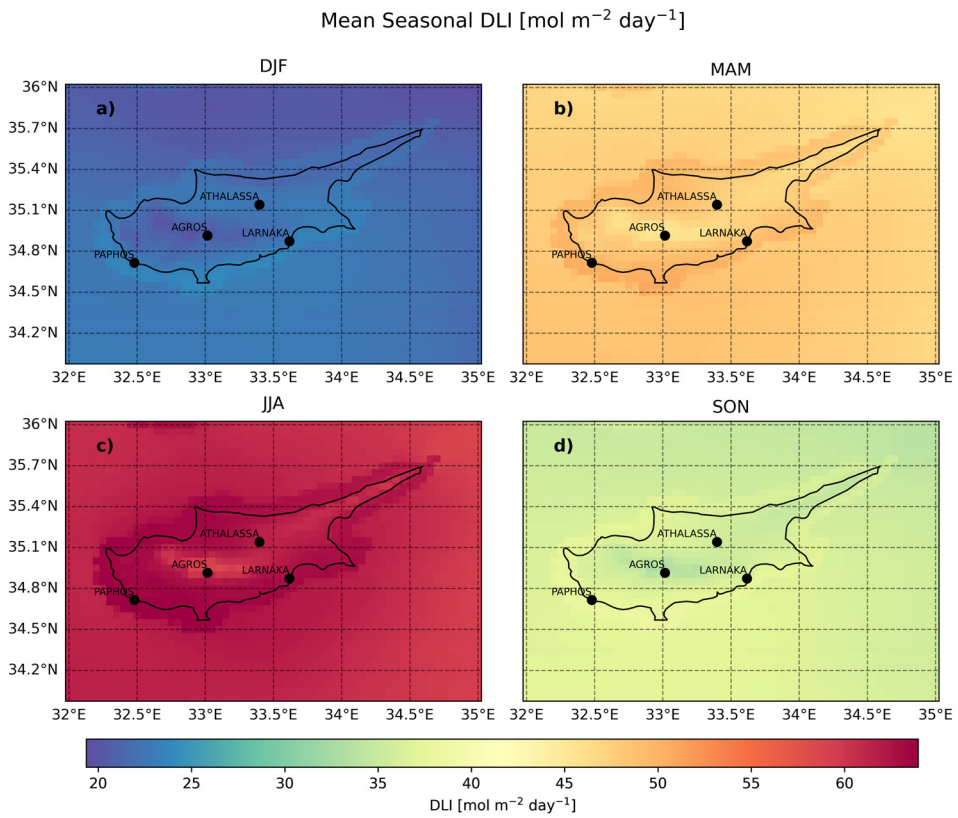

Figure A2. Same as Figure A1 but for DLI.

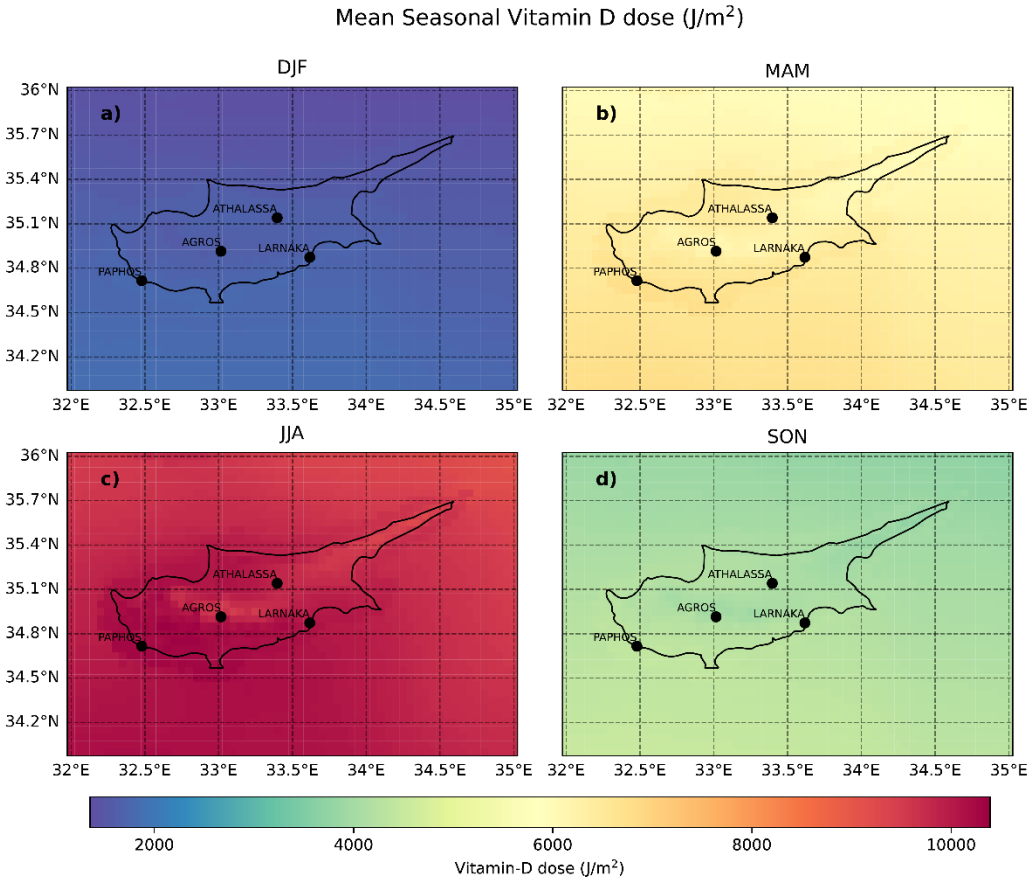

Figure A3. Same as Figure A1 for Vitamin D doses.

Preprints.org (www.preprints.org) | NOT PEER-REVIEWED | Posted: 5 April 2024 doi:10.20944/preprints202404.0431.v1

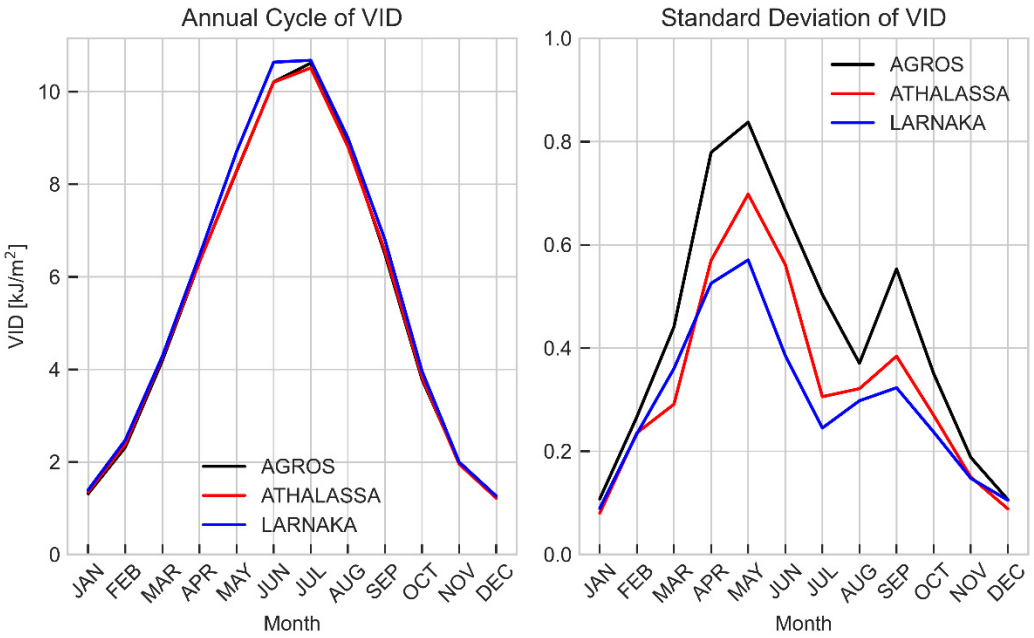

Figure A4. Monthly average Vitamin D dose for the period 2004 – 2023 for Agros, Athalassa, and Larnaka (left panel), and the corresponding standard deviation (right panel).

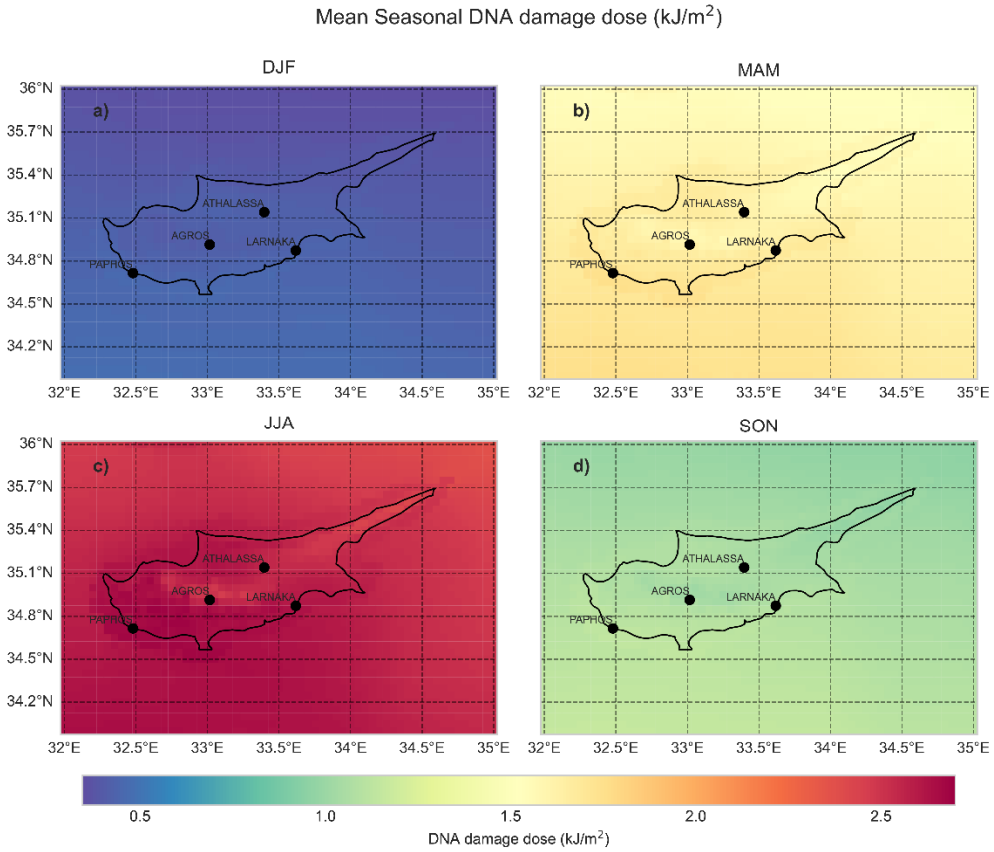

Figure A5. Same as Figure A1 for dna damage.

Preprints.org (www.preprints.org) | NOT PEER-REVIEWED | Posted: 5 April 2024 doi:10.20944/preprints202404.0431.v1

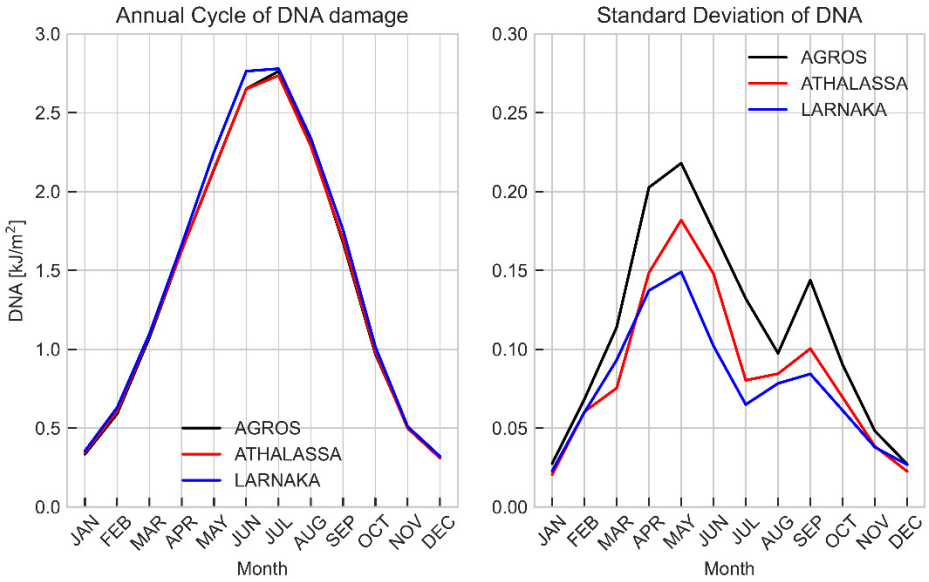

Figure A6. Same as Figure A4 for dna damage.

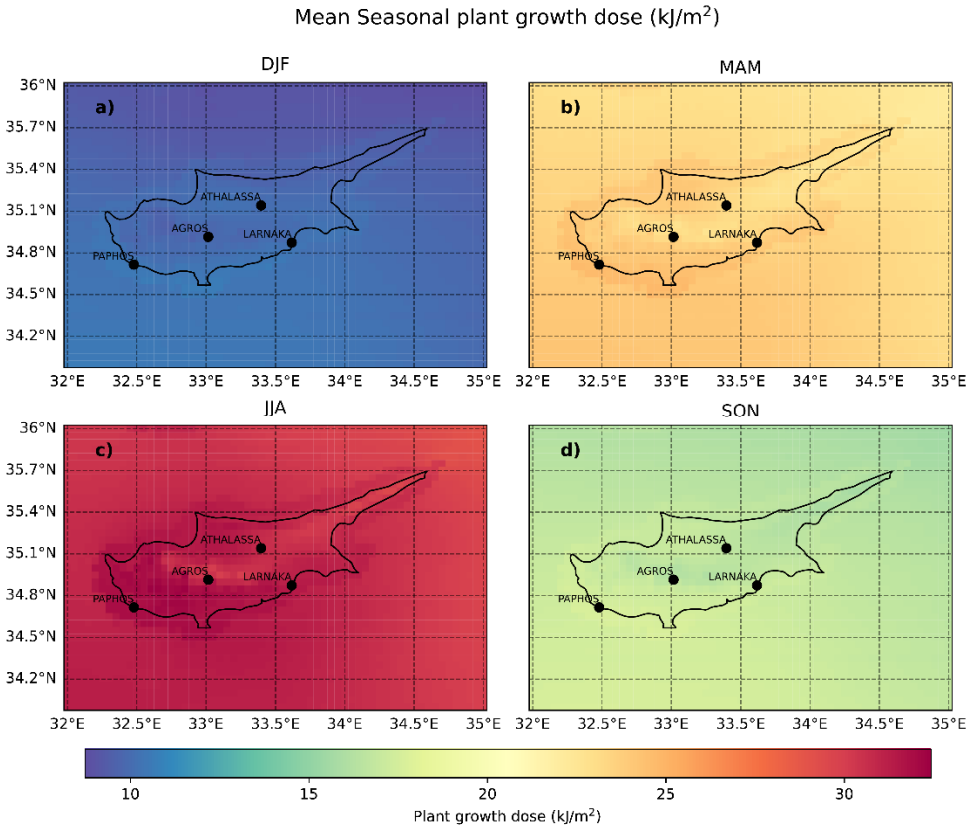

Figure A7. Same as Figure A1 for plant growth.

Preprints.org (www.preprints.org) | NOT PEER-REVIEWED | Posted: 5 April 2024 doi:10.20944/preprints202404.0431.v1

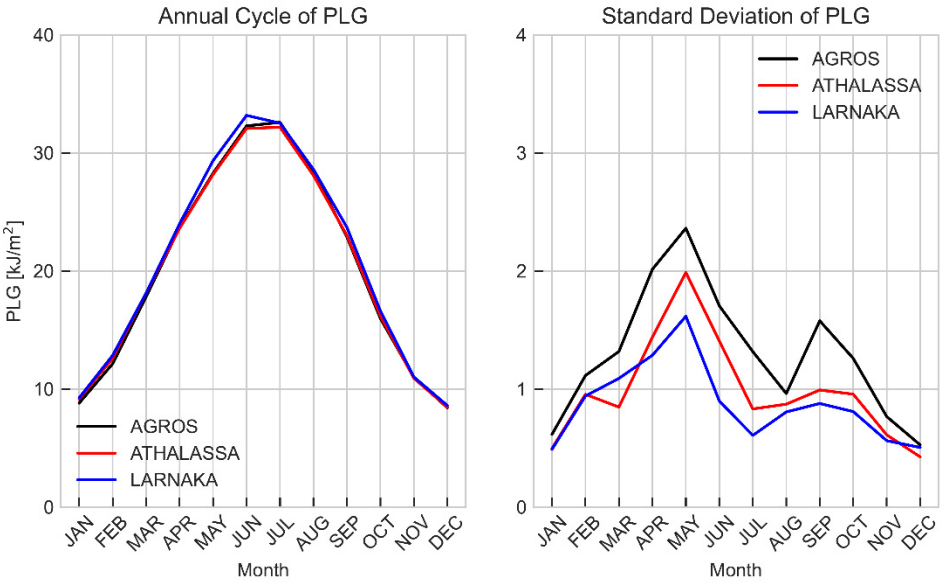

Figure A8. Same as Figure A4 for plant growth.

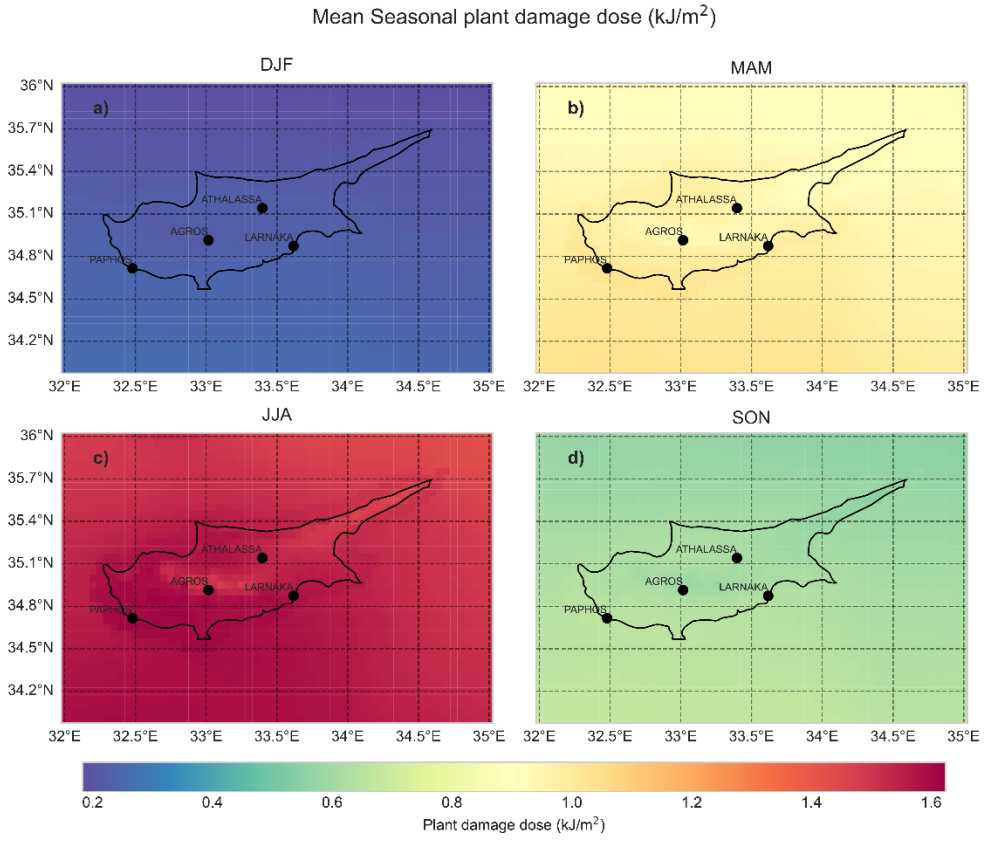

Figure A9. Same as Figure A1 for plant damage.

 doi:10.20944/preprints202404.0431.v1

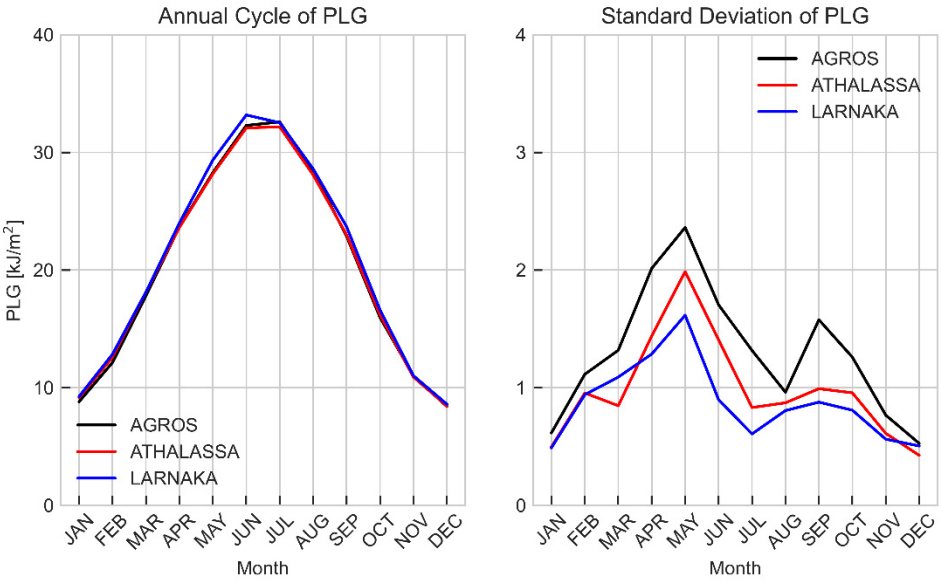

Figure A10. Same as Figure A4 for plant damage.

References

1. McCree, K.J. Photosynthetically Active Radiation. In *Physiological Plant Ecology I: Responses to the Physical Environment*; Lange O. L. and Nobel, P.S. and O.C.B. and Z.H., Ed.; Springer Berlin Heidelberg: Berlin, Heidelberg, 1981; pp. 41–55 ISBN 978-3-642-68090-8.
2. McCree, K.J. Test of Current Definitions of Photosynthetically Active Radiation against Leaf Photosynthesis Data. *Agricultural Meteorology* **1972**, *10*, 443–453, doi:https://doi.org/10.1016/0002-1571(72)90045-3.
3. Alados, I.; Foyo-Moreno, I.; Alados-Arboledas, L. Photosynthetically Active Radiation: Measurements and Modelling. *Agric For Meteorol* **1996**, *78*, 121–131, doi:https://doi.org/10.1016/0168-1923(95)02245-7.
4. Fu, F.X.; Tatters, A.O.; Hutchins, D.A. Global Change and the Future of Harmful Algal Blooms in the Ocean. *Mar Ecol Prog Ser* **2012**, *470*, 207–233, doi:10.3354/meps10047.
5. Lesser, M.P.; Farrell, J.H. Exposure to Solar Radiation Increases Damage to Both Host Tissues and Algal Symbionts of Corals during Thermal Stress. *Coral Reefs* **2004**, *23*, 367–377, doi:10.1007/s00338-004-0392-z.
6. Chukwujindu Nwokolo, S.; Ogbulezie, J.C.; Umunnakwe Obiwulu, A. Impacts of Climate Change and Meteo-Solar Parameters on Photosynthetically Active Radiation Prediction Using Hybrid Machine Learning with Physics-Based Models. *Advances in Space Research* **2022**, *70*, 3614–3637, doi:10.1016/j.asr.2022.08.010.
7. Thomas, C.; Wandji Nyamsi, W.; Arola, A.; Pfeifroth, U.; Trentmann, J.; Dorling, S.; Laguarda, A.; Fischer, M.; Aculinin, A. Smart Approaches for Evaluating Photosynthetically Active Radiation at Various Stations Based on MSG Prime Satellite Imagery. *Atmosphere (Basel)* **2023**, *14*, doi:10.3390/atmos14081259.
8. Aguiar, L.J.G.; Fischer, G.R.; Ladle, R.J.; Malhado, A.C.M.; Justino, F.B.; Aguiar, R.G.; da Costa, J.M.N. Modeling the Photosynthetically Active Radiation in South West Amazonia under All Sky Conditions. *Theor Appl Climatol* **2012**, *108*, 631–640, doi:10.1007/s00704-011-0556-z.
9. Zempila, M.-M.; Taylor, M.; Bais, A.; Kazadzis, S. Modeling the Relationship between Photosynthetically Active Radiation and Global Horizontal Irradiance Using Singular Spectrum Analysis. *J Quant Spectrosc Radiat Transf* **2016**, *182*, 240–263, doi:https://doi.org/10.1016/j.jqsrt.2016.06.003.
10. Sun, Z.; Liang, H.; Liu, J.; Shi, G. Estimation of Photosynthetically Active Radiation Using Solar Radiation in the UV–Visible Spectral Band. *Solar Energy* **2017**, *153*, 611–622, doi:https://doi.org/10.1016/j.solener.2017.06.007.
11. de Blas, M.; García-Rodríguez, A.; García, I.; Torres, J.L. Validation and Calibration of Models to Estimate Photosynthetically Active Radiation Considering Different Time Scales and Sky Conditions. *Advances in Space Research* **2022**, *70*, 1737–1760, doi:https://doi.org/10.1016/j.asr.2022.07.005.
12. Thomas, C.; Wandji Nyamsi, W.; Arola, A.; Pfeifroth, U.; Trentmann, J.; Dorling, S.; Laguarda, A.; Fischer, M.; Aculinin, A. Smart Approaches for Evaluating Photosynthetically Active Radiation at Various Stations Based on MSG Prime Satellite Imagery. *Atmosphere (Basel)* **2023**, *14*, doi:10.3390/atmos14081259.
13. Liou, K.-N. *An Introduction to Atmospheric Radiation*; Elsevier, 2002; Vol. 84;.
14. Brasseur, G.; Simon, P.C. Stratospheric Chemical and Thermal Response to Long-Term Variability in Solar UV Irradiance. *J Geophys Res* **1981**, *86*, 7343–7362, doi:10.1029/jc086ic08p07343.

15. Brasseur, G.; De Rudder, A.; Keating, G.M.; Pitts, M.C. Response of Middle Atmosphere to Short-Term Ultraviolet Variations: 2. Theory. *J Geophys Res* **1987**, *92*, 903–914, doi:10.1029/JD092iD01p00903.
16. Lucas, R.M.; Yazar, S.; Young, A.R.; Norval, M.; De Gruijl, F.R.; Takizawa, Y.; Rhodes, L.E.; Sinclair, C.A.; Neale, R.E. Human Health in Relation to Exposure to Solar Ultraviolet Radiation under Changing Stratospheric Ozone and Climate. *Photochemical and Photobiological Sciences* **2019**, *18*, 641–680, doi:10.1039/C8PP90060D.
17. Zerefos, C.; Fountoulakis, I.; Eleftheratos, K.; Kazantzidis, A. Long-Term Variability of Human Health-Related Solar Ultraviolet-B Radiation Doses from the 1980s to the End of the 21st Century. *Physiol Rev* **2023**, *103*, 1789–1826, doi:10.1152/physrev.00031.2022.
18. Diffey, B.L. Solar Ultraviolet Radiation Effects on Biological Systems. *Phys Med Biol* **1991**, *36*, 299–328, doi:10.1088/0031-9155/36/3/001.
19. McKinlay, A.F. REFERENCE ACTION SPECTRUM FOR ULTRAVIOLET INDUCED ERYTHEMA IN HUMAN SKIN. *CIE-journal* **1987**, *6*, 17–22.
20. Setlow, R.B. The Wavelengths in Sunlight Effective in Producing Skin Cancer: A Theoretical Analysis. *Proc Natl Acad Sci U S A* **1974**, *71*, doi:10.1073/pnas.71.9.3363.
21. WHO Health and Environmental Effects of Ultraviolet Radiation:A Scientific Summary of Environmental Health Criteria 160 Ultraviolet Radiation ((WHO/EHG/95.16). *World Health Organization* 1994.
22. Taylor, H.R.; West, S.K.; Rosenthal, F.S.; Muñoz, B.; Newland, H.S.; Abbey, H.; Emmett, E.A. Effect of Ultraviolet Radiation on Cataract Formation. *New England Journal of Medicine* **1988**, *319*, doi:10.1056/nejm198812013192201.
23. Jablonski, N.G.; Chaplin, G. The Evolution of Human Skin Coloration. *J Hum Evol* **2000**, *39*, doi:10.1006/jhev.2000.0403.
24. Juzeniene, A.; Brekke, P.; Dahlback, A.; Andersson-Engels, S.; Reichrath, J.; Moan, K.; Holick, M.F.; Grant, W.B.; Moan, J. Solar Radiation and Human Health. *Reports on Progress in Physics* **2011**, *74*, doi:10.1088/0034-4885/74/6/066701.
25. Holick, M.F. High Prevalence of Vitamin D Inadequacy and Implications for Health. *Mayo Clin Proc* 2006, *81*.
26. Juzeniene, A.; Moan, J. Beneficial Effects of UV Radiation Other than via Vitamin D Production. *Dermatoendocrinol* 2012, *4*.
27. Vanicek, K.; Frei, T. UV- Index for the Public. *Publication of the European Communities, Brussels, Belgium* **2005**.
28. CIE *Action Spectrum for the Production of Previtamin D3 in Human Skin (CIE Publication 174, ISBN 3 901 906 50 9)*; 2006;
29. Kazantzidis, A.; Bais, A.F.; Zempila, M.M.; Kazadzis, S.; Den Outer, P.N.; Koskela, T.; Slaper, H. Calculations of the Human Vitamin D Exposure from UV Spectral Measurements at Three European Stations. *Photochemical and Photobiological Sciences* **2009**, *8*, doi:10.1039/b811216a.
30. Lucas, R.M.; Yazar, S.; Young, A.R.; Norval, M.; De Gruijl, F.R.; Takizawa, Y.; Rhodes, L.E.; Sinclair, C.A.; Neale, R.E. Human Health in Relation to Exposure to Solar Ultraviolet Radiation under Changing Stratospheric Ozone and Climate. *Photochemical and Photobiological Sciences* **2019**, *18*, 641–680, doi:10.1039/C8PP90060D.
31. Webb, A.R.; Kazantzidis, A.; Kift, R.C.; Farrar, M.D.; Wilkinson, J.; Rhodes, L.E. Colour Counts: Sunlight and Skin Type as Drivers of Vitamin D Deficiency at UK Latitudes. *Nutrients* **2018**, *10*, doi:10.3390/nu10040457.
32. Schreiner, M.; Mewis, I.; Huyskens-Keil, S.; Jansen, M.A.K.; Zrenner, R.; Winkler, J.B.; O'Brien, N.; Krumbein, A. UV-B-Induced Secondary Plant Metabolites - Potential Benefits for Plant and Human Health. *CRC Crit Rev Plant Sci* **2012**, *31*, doi:10.1080/07352689.2012.664979.
33. Kataria, S.; Jajoo, A.; Guruprasad, K.N. Impact of Increasing Ultraviolet-B (UV-B) Radiation on Photosynthetic Processes. *J Photochem Photobiol B* **2014**, *137*, doi:10.1016/j.jphotobiol.2014.02.004.
34. Frohnmeyer, H.; Staiger, D. Ultraviolet-B Radiation-Mediated Responses in Plants. Balancing Damage and Protection. *Plant Physiol* 2003, *133*.
35. Zerefos, C.S.; Bais, A.F.; Meleti, C.; Ziomas, I.C. A Note on the Recent Increase of Solar UV-B Radiation over Northern Middle Latitudes. *Geophys Res Lett* **1995**, *22*, doi:10.1029/95GL01187.
36. Kerr, J.B.; McElroy, C.T. Evidence for Large Upward Trends of Ultraviolet-B Radiation Linked to Ozone Depletion. *Science (1979)* **1993**, *262*, doi:10.1126/science.262.5136.1032.
37. Lubin, D.; Jensen, E.H. Effects of Clouds and Stratospheric Ozone Depletion on Ultraviolet Radiation Trends. *Nature* **1995**, *377*, doi:10.1038/377710a0.
38. Madronich, S.; McKenzie, R.L.; Björn, L.O.; Caldwell, M.M. Changes in Biologically Active Ultraviolet Radiation Reaching the Earth's Surface. *J Photochem Photobiol B* **1998**, *46*, doi:10.1016/S1011-1344(98)00182-1.
39. Madronich, S. Implications of Recent Total Atmospheric Ozone Measurements for Biologically Active Ultraviolet Radiation Reaching the Earth's Surface. *Geophys Res Lett* **1992**, *19*, doi:10.1029/91GL02954.

40. Godin-Beekmann, S.; Azouz, N.; Sofieva, V.F.; Hubert, D.; Petropavlovskikh, I.; Effertz, P.; Ancellet, G.; Degenstein, D.A.; Zawada, D.; Froidevaux, L.; et al. Updated Trends of the Stratospheric Ozone Vertical Distribution in the 60°S-60°N Latitude Range Based on the LOTUS Regression Model. *Atmos Chem Phys* **2022**, *22*, doi:10.5194/acp-22-11657-2022.
41. Fountoulakis, I.; Diémoz, H.; Siani, A.M.; Di Sarra, A.; Meloni, D.; Sferlazzo, D.M. Variability and Trends in Surface Solar Spectral Ultraviolet Irradiance in Italy: On the Influence of Geopotential Height and Lower-Stratospheric Ozone. *Atmos Chem Phys* **2021**, *21*, doi:10.5194/acp-21-18689-2021.
42. Fountoulakis, I.; Bais, A.F.; Fragkos, K.; Meleti, C.; Tourpali, K.; Maria Zempila, M. Short- and Long-Term Variability of Spectral Solar UV Irradiance at Thessaloniki, Greece: Effects of Changes in Aerosols, Total Ozone and Clouds. *Atmos Chem Phys* **2016**, *16*, doi:10.5194/acp-16-2493-2016.
43. Fountoulakis, I.; Diémoz, H.; Siani, A.M.; Laschewski, G.; Filippa, G.; Arola, A.; Bais, A.F.; Backer, H. De; Lakkala, K.; Webb, A.R.; et al. Solar UV Irradiance in a Changing Climate: Trends in Europe and the Significance of Spectral Monitoring in Italy. *Environments - MDPI* **2020**, *7*, doi:10.3390/environments7010001.
44. Meleti, C.; Bais, A.F.; Kouremeti, N.; Garane, K.; Kazadzis, S.; Zerefos, C. Factors Affecting Solar Ultraviolet Irradiance Measured since 1990 at Thessaloniki, Greece. *Int J Remote Sens* **2009**, *30*, doi:10.1080/01431160902822864.
45. Zerefos, C.S.; Tourpali, K.; Eleftheratos, K.; Kazadzis, S.; Meleti, C.; Feister, U.; Koskela, T.; Heikkilä, A. Evidence of a Possible Turning Point in Solar UV-B over Canada, Europe and Japan. *Atmos Chem Phys* **2012**, *12*, doi:10.5194/acp-12-2469-2012.
46. De Bock, V.; De Backer, H.; Van Malderen, R.; Mangold, A.; Delcloo, A. Relations between Erythemal UV Dose, Global Solar Radiation, Total Ozone Column and Aerosol Optical Depth at Uccle, Belgium. *Atmos Chem Phys* **2014**, *14*, doi:10.5194/acp-14-12251-2014.
47. Kambezidis, H.D. The Solar Radiation Climate of Athens: Variations and Tendencies in the Period 1992–2017, the Brightening Era. *Solar Energy* **2018**, *173*, doi:10.1016/j.solener.2018.07.076.
48. Wild, M.; Wacker, S.; Yang, S.; Sanchez-Lorenzo, A. Evidence for Clear-Sky Dimming and Brightening in Central Europe. *Geophys Res Lett* **2021**, *48*, doi:10.1029/2020GL092216.
49. Manara, V.; Bassi, M.; Brunetti, M.; Cagnazzi, B.; Maugeri, M. 1990–2016 Surface Solar Radiation Variability and Trend over the Piedmont Region (Northwest Italy). *Theor Appl Climatol* **2019**, *136*, doi:10.1007/s00704-018-2521-6.
50. Papachristopoulou, K.; Fountoulakis, I.; Gkikas, A.; Kosmopoulos, P.G.; Nastos, P.T.; Hatzaki, M.; Kazadzis, S. 15-Year Analysis of Direct Effects of Total and Dust Aerosols in Solar Radiation/Energy over the Mediterranean Basin. *Remote Sens (Basel)* **2022**, *14*, doi:10.3390/rs14071535.
51. Kazadzis, S.; Founda, D.; Psiloglou, B.E.; Kambezidis, H.; Mihalopoulos, N.; Sanchez-Lorenzo, A.; Meleti, C.; Raptis, P.I.; Pierros, F.; Nabat, P. Long-Term Series and Trends in Surface Solar Radiation in Athens, Greece. *Atmos Chem Phys* **2018**, *18*, doi:10.5194/acp-18-2395-2018.
52. Cos, J.; Doblas-Reyes, F.; Jury, M.; Marcos, R.; Bretonnière, P.A.; Samsó, M. The Mediterranean Climate Change Hotspot in the CMIP5 and CMIP6 Projections. *Earth System Dynamics* **2022**, *13*, doi:10.5194/esd-13-321-2022.
53. Tuel, A.; Eltahir, E.A.B. Why Is the Mediterranean a Climate Change Hot Spot? *J Clim* **2020**, *33*, doi:10.1175/JCLI-D-19-0910.1.
54. Fountoulakis, I.; Kosmopoulos, P.; Papachristopoulou, K.; Raptis, I.-P.; Mamouri, R.-E.; Nisantzi, A.; Gkikas, A.; Witthuhn, J.; Bley, S.; Moustaka, A.; et al. Effects of Aerosols and Clouds on the Levels of Surface Solar Radiation and Solar Energy in Cyprus. *Remote Sens (Basel)* **2021**, *13*, doi:10.3390/rs13122319.
55. Jacovides, C.P.; Tymvios, F.S.; Asimakopoulos, D.N.; Theofilou, K.M.; Pashiardes, S. Global Photosynthetically Active Radiation and Its Relationship with Global Solar Radiation in the Eastern Mediterranean Basin. *Theor Appl Climatol* **2003**, *74*, doi:10.1007/s00704-002-0685-5.
56. Kalogirou, S.A.; Pashiardis, S.; Pashiardi, A. Statistical Analysis and Inter-Comparison of Erythemal Solar Radiation for Athalassa and Larnaca, Cyprus. *Renew Energy* **2017**, *111*, 580–597, doi:10.1016/j.renene.2017.04.043.
57. Kalogirou, S.A.; Pashiardis, S.; Pashiardi, A. Statistical Analysis and Inter-Comparison of the Global Solar Radiation at Two Sites in Cyprus. *Renew Energy* **2017**, *101*, doi:10.1016/j.renene.2016.09.027.
58. Pashiardis, S.; Kalogirou, S.A.; Pelengaris, A. Statistical Analysis for the Characterization of Solar Energy Utilization and Inter-Comparison of Solar Radiation at Two Sites in Cyprus. *Appl Energy* **2017**, *190*, doi:10.1016/j.apenergy.2017.01.018.
59. Webb, A.R.; Slaper, H.; Koepke, P.; Schmalwieser, A.W. Know Your Standard: Clarifying the CIE Erythema Action Spectrum. *Photochem Photobiol* **2011**, *87*, doi:10.1111/j.1751-1097.2010.00871.x.
60. Setlow, R.B. The Wavelengths in Sunlight Effective in Producing Skin Cancer: A Theoretical Analysis. *Proc Natl Acad Sci U S A* **1974**, *71*, 3363–3366, doi:10.1073/pnas.71.9.3363.
61. Bernhard, G.; Mayer, B.; Seckmeyer, G.; Moise, A. Measurements of Spectral Solar UV Irradiance in Tropical Australia. *Journal of Geophysical Research Atmospheres* **1997**, *102*, doi:10.1029/97jd00072.
62. Caldwell, M.M. Plant Response to Solar Ultraviolet Radiation. In *Physiological Plant Ecology I*; 1981.

63. Caldwell, M.M. Plant Life and Ultraviolet Radiation: Some Perspective in the History of the Earth's UV Climate. *Bioscience* **1979**, *29*, doi:10.2307/1307719.
64. Emde, C.; Buras-Schnell, R.; Kylling, A.; Mayer, B.; Gasteiger, J.; Hamann, U.; Kylling, J.; Richter, B.; Pause, C.; Dowling, T.; et al. The LibRadtran Software Package for Radiative Transfer Calculations (Version 2.0.1). *Geosci Model Dev* **2016**, *9*, 1647–1672, doi:10.5194/gmd-9-1647-2016.
65. Mayer, B.; Kylling, A. Technical Note: The LibRadtran Software Package for Radiative Transfer Calculations - Description and Examples of Use. *Atmos Chem Phys* **2005**, *5*, 1855–1877, doi:10.5194/acp-5-1855-2005.
66. Buras, R.; Dowling, T.; Emde, C. New Secondary-Scattering Correction in DISORT with Increased Efficiency for Forward Scattering. *J Quant Spectrosc Radiat Transf* **2011**, *112*, doi:10.1016/j.jqsrt.2011.03.019.
67. Gasteiger, J.; Emde, C.; Mayer, B.; Buras, R.; Buehler, S.A.; Lemke, O. Representative Wavelengths Absorption Parameterization Applied to Satellite Channels and Spectral Bands. *J Quant Spectrosc Radiat Transf* **2014**, *148*, doi:10.1016/j.jqsrt.2014.06.024.
68. Anderson, G. and C.S. and K.F. and C.J. and S.E. *AFGL (Air Force Geophysical Laboratory) Atmospheric Constituent Profiles (0. 120km). Environmental Research Papers*; 1986;
69. Kurucz, R.L. Synthetic Infrared Spectra. *Symposium - International Astronomical Union* **1994**, *154*, doi:10.1017/s0074180900124805.
70. Shettle, E.P. Models of Aerosols, Clouds and Precipitation for Atmospheric Propagation Studies. *AGARD Conf.* **1989**.
71. Zempila, M.M.; Van Geffen, J.H.G.M.; Taylor, M.; Fountoulakis, I.; Koukouli, M.E.; Van Weele, M.; Van Der A, R.J.; Bais, A.; Meleti, C.; Balis, D. TEMIS UV Product Validation Using NILU-UV Ground-Based Measurements in Thessaloniki, Greece. *Atmos Chem Phys* **2017**, *17*, doi:10.5194/acp-17-7157-2017.
72. Qu, Z.; Oumbe, A.; Blanc, P.; Espinar, B.; Gesell, G.; Gschwind, B.; Klüser, L.; Lefèvre, M.; Saboret, L.; Schroedter-Homscheidt, M.; et al. Fast Radiative Transfer Parameterisation for Assessing the Surface Solar Irradiance: The Heliosat-4 Method. *Meteorologische Zeitschrift* **2017**, *26*, doi:10.1127/metz/2016/0781.
73. Lefèvre, M.; Oumbe, A.; Blanc, P.; Espinar, B.; Gschwind, B.; Qu, Z.; Wald, L.; Schroedter-Homscheidt, M.; Hoyer-Klick, C.; Arola, A.; et al. McClear: A New Model Estimating Downwelling Solar Radiation at Ground Level in Clear-Sky Conditions. *Atmos Meas Tech* **2013**, *6*, doi:10.5194/amt-6-2403-2013.
74. Staiger, H.; Den Outer, P.N.; Bais, A.F.; Feister, U.; Johnsen, B.; Vuilleumier, L. Hourly Resolved Cloud Modification Factors in the Ultraviolet. *Atmos Chem Phys* **2008**, *8*, doi:10.5194/acp-8-2493-2008.
75. Inness, A.; Ades, M.; Agustí-Panareda, A.; Barr, J.; Benedictow, A.; Blechschmidt, A.M.; Jose Dominguez, J.; Engelen, R.; Eskes, H.; Flemming, J.; et al. The CAMS Reanalysis of Atmospheric Composition. *Atmos Chem Phys* **2019**, *19*, doi:10.5194/acp-19-3515-2019.
76. Kinne, S. The MACv2 Aerosol Climatology. *Tellus B Chem Phys Meteorol* **2019**, *71*, doi:10.1080/16000889.2019.1623639.
77. Veefkind, J.P.; de Haan, J.F.; Brinksma, E.J.; Kroon, M.; Levelt, P.F. Total Ozone from the Ozone Monitoring Instrument (OMI) Using the DOAS Technique. *IEEE Transactions on Geoscience and Remote Sensing* **2006**, *44*, 1239–1244, doi:10.1109/TGRS.2006.871204.
78. McCree, K.J. The Action Spectrum, Absorptance and Quantum Yield of Photosynthesis in Crop Plants. *Agricultural Meteorology* **1971**, *9*, doi:10.1016/0002-1571(71)90022-7.
79. Thimijan, R.W.; Heins, R.D. Photometric, Radiometric, and Quantum Light Units of Measure: A Review of Procedures for Interconversion. *HortScience* **1983**, *18*, 818–822, doi:10.21273/HORTSCI.18.6.818.
80. Korczynski, P.C.; Logan, J.; Faust, J.E. Mapping Monthly Distribution of Daily Light Integrals across the Contiguous United States. *Horttechnology* 2002, *12*.
81. Pfeifroth, U.; Kothe, S.; Drücke, J.; Trentmann, J.; Schröder, M.; Selbach, N.; Hollmann, R. Surface Radiation Data Set - Heliosat (SARAH) - Edition 3 2023.
82. Mueller, R.; Behrendt, T.; Hammer, A.; Kemper, A. A New Algorithm for the Satellite-Based Retrieval of Solar Surface Irradiance in Spectral Bands. *Remote Sens (Basel)* **2012**, *4*, 622–647, doi:10.3390/rs4030622.
83. Van Geffen, J.; Van Weele, M.; Allaart, M.; Van der A, R. Dataset: TEMIS UV Index and UV Dose Operational Data Products, Version 2. 2017.
84. Greene, W.W.H.. *Econometric Analysis 7th Ed*; 2012; Vol. 97;.

 doi:10.20944/preprints202404.0431.v1

85. Nisantzi, A.; Mamouri, R.E.; Ansmann, A.; Schuster, G.L.; Hadjimitsis, D.G. Middle East versus Saharan Dust Extinction-to-Backscatter Ratios. *Atmos Chem Phys* **2015**, *15*, doi:10.5194/acp-15-7071-2015.
86. Achilleos, S.; Mouzourides, P.; Kalivitis, N.; Katra, I.; Kloog, I.; Kouis, P.; Middleton, N.; Mihalopoulos, N.; Neophytou, M.; Panayiotou, A.; et al. Spatio-Temporal Variability of Desert Dust Storms in Eastern Mediterranean (Crete, Cyprus, Israel) between 2006 and 2017 Using a Uniform Methodology. *Science of the Total Environment* **2020**, *714*, doi:10.1016/j.scitotenv.2020.136693.